AGU PUBLICATIONS

JGR

Journal of Geophysical Research: Earth Surface

RESEARCH ARTICLE
10.1002/2014JF003412

Key Points:
- Flow convergence at waterfalls increases flow velocity, bed stress, and discharge
- Convergence is strong for laterally extensive, subcritical floods
- Wall effects and drawdown hydrodynamics may set waterfall width

Correspondence to:
M. G. A. Lapotre,
mlapotre@caltech.edu

Citation:
Lapotre, M. G. A., and M. P. Lamb (2015), Hydraulics of floods upstream of horseshoe canyons and waterfalls, *J. Geophys. Res. Earth Surf.*, *120*, 1227–1250, doi:10.1002/2014JF003412.

Received 10 DEC 2014
Accepted 11 MAY 2015
Accepted article online 11 MAY 2015
Published online 14 JUL 2015

Hydraulics of floods upstream of horseshoe canyons and waterfalls

Mathieu G. A. Lapotre[1] and Michael P. Lamb[1]

[1]Division of Geological and Planetary Sciences, California Institute of Technology, Pasadena, California, USA

Abstract Horseshoe waterfalls are ubiquitous in natural streams, bedrock canyons, and engineering structures. Nevertheless, water flow patterns upstream of horseshoe waterfalls are poorly known and likely differ from the better studied case of a one-dimensional linear step because of flow focusing into the horseshoe. This is a significant knowledge gap because the hydraulics at waterfalls controls sediment transport and bedrock incision, which can compromise the integrity of engineered structures and influence the evolution of river canyons on Earth and Mars. Here we develop new semiempirical theory for the spatial acceleration of water upstream of, and the cumulative discharge into, horseshoe canyons and waterfalls. To this end, we performed 110 numerical experiments by solving the 2-D depth-averaged shallow-water equations for a wide range of flood depths, widths and discharges, and canyon lengths, widths and bed gradients. We show that the upstream, normal flow Froude number is the dominant control on lateral flow focusing and acceleration into the canyon head and that focusing is limited when the flood width is small compared to a cross-stream backwater length scale. In addition, for sheet floods much wider than the canyon, flow focusing into the canyon head leads to reduced discharge (and drying in cases) across the canyon sidewalls, which is especially pronounced for canyons that are much longer than they are wide. Our results provide new expectations for morphodynamic feedbacks between floods and topography, and thus canyon formation.

1. Introduction

The hydraulics of waterfalls have been studied for over a century [e.g., *Bresse*, 1860], largely in response to the development of dams and other engineered structures [e.g., *Chanson*, 1994, 1995, 2002] (Figure 1f). In addition to their importance in hydraulic engineering, waterfalls play a major role in channel erosion [*Flint*, 1973; *Dietrich and Dunne*, 1993] and often form because of changes in climate, tectonics, and sea level [*Brush and Wolman*, 1960; *Leopold and Bull*, 1979; *Gardner*, 1983; *Howard et al.*, 1994; *Bishop et al.*, 2005; *DiBiase et al.*, 2014; *Lamb et al.*, 2014; *Mackey et al.*, 2014]. Waterfalls on Earth (Figures 1d, 1g, and 1h) [*Gilbert*, 1907], but also dry cataracts on Earth and Mars (Figures 1e, 1i, and 1j), are often horseshoe shaped and create canyons with amphitheater-shaped heads [*Bretz*, 1969; *Baker and Milton*, 1974; *O'Connor*, 1993; *Lamb et al.*, 2008, 2014; *Warner et al.*, 2010; *DiBiase et al.*, 2014; *Baynes et al.*, 2015]. This geometry is observed at various scales, from decimeter-scale rills (Figure 1c) to meter-scale rivers and channel heads (Figures 1a, 1b, and 1h) to hundreds of meters to kilometer-scale megaflood canyons (Figures 1e, 1i, and 1j).

The horseshoe shape of waterfalls likely influences plan view flow patterns upstream by focusing water toward the center of the horseshoe [e.g., *Pasternack et al.*, 2006, 2007]. Water accelerates as it moves toward a waterfall due to the reduction in pressure to atmospheric at the waterfall brink. Acceleration and lateral flow convergence (i.e., flow focusing) control the velocity, discharge, and size of the jet impinging in the plunge pool [*Chanson*, 1994; *Flores-Cervantes et al.*, 2006; *Tokyay and Yildiz*, 2007], which ultimately sets the pace of undercutting and potential collapse of the cliff face [*Dietrich and Dunne*, 1993; *Stein et al.*, 1993; *Alonso et al.*, 2002; *Stein and LaTray*, 2002; *Lamb et al.*, 2007]. Flow acceleration also enhances the bed shear stress exerted by the flow at the waterfall brink [*Stein and Julien*, 1993; *Haviv et al.*, 2006] and thus promotes plucking and toppling of jointed rock [*Annandale*, 1995; *Hancock et al.*, 1998; *Whipple et al.*, 2000; *Coleman et al.*, 2003; *Wohl*, 2008; *Chatanantavet and Parker*, 2009; *Lamb and Dietrich*, 2009; *Dubinski and Wohl*, 2013]. Moreover, larger flow discharges into canyon heads allow transport of larger sediment and higher sediment transport rates downstream of the waterfall as long as sediment is available [*Meyer-Peter and Muller*, 1948; *Fernandez Luque and Van Beek*, 1976], which exert important controls on the stability of engineering dams and spillways, as well as canyon evolution over

Figure 1. (a) Undercut horseshoe heads carved by overland flow in the Keanakāko'i thephra, Ka'ū desert, Kīlauea volcano, Hawai'i [e.g., *Craddock et al.*, 2012]. (b) Gully head near West Bijou Creek, Colorado, USA [e.g., *Tucker et al.*, 2006; *Rengers and Tucker*, 2014]. (c) Undercut horseshoe-shaped rill carved by overland flow on noncohesive soil in Gower Gulch, Death Valley. (d) Niagara Falls, New York, USA (Credit: Helen Filatova, released under CC-BY-SA-3.0). (e) View of the head of Stubby Canyon, Malad Gorge State Park, Idaho, USA, from the canyon floor [*Lamb et al.*, 2014]. (f) Horseshoe weir, Bath, UK (Credit: Jurgen Matern, released under CC-BY-SA-3.0). (g) Selfoss waterfall on the Jökulsá á Fjöllum river, Iceland (Credit: Hansueli Krapf, released under CC-BY-SA-3.0). (h) Amphitheater-headed waterfall near Potholes Reservoir, Potholes State Park, Washington, USA. (i) CTX mosaic of an amphitheater-shaped canyon at Echus Chasma (Credit: NASA). (j) HiRISE image of an amphitheater-shaped cataract within Kasei Valles (PSP_002788_2010) [e.g., *Williams and Malin*, 2004].

longer timescales [e.g., *Lamb et al.*, 2006]. *Petroff et al.* [2011] argued that amphitheater-headed canyons may arise from any erosional process for which erosion rate is proportional to plan view curvature of the escarpment. Nevertheless, whether the erosion rate at waterfalls is proportional to the plan view curvature is yet to be shown. Investigating the hydraulics of waterfall escarpments is a necessary first step to mechanistic theories for canyon head and waterfall erosion [e.g., *Lamb and Dietrich*, 2009]. Lateral focusing of flow upstream of waterfalls may also influence the development of drainage networks (e.g., canyon spacing) driven by upstream canyon head retreat [*Izumi and Parker*, 1995, 2000]. Despite its importance, flow focusing upstream and into horseshoe waterfalls has yet to be studied systematically, a knowledge gap we aim to address herein.

Most work to quantify flow acceleration upstream of waterfalls is for linear escarpments with no topographic variation across the channel width and hence is essentially 1-D [*Rouse*, 1936, 1937, 1950; *Delleur et al.*, 1956; *Rajaratnam and Muralidhar*, 1968; *Hager*, 1983; *Hager and Hutter*, 1984]. The acceleration factor in 1-D is defined as $\alpha_{1D} = U_0/U_n$, where U_0 is the velocity at the waterfall brink and U_n is the normal flow velocity in the downstream direction [*Rouse*, 1936]. Normal flow is defined as steady and uniform flow (i.e., far

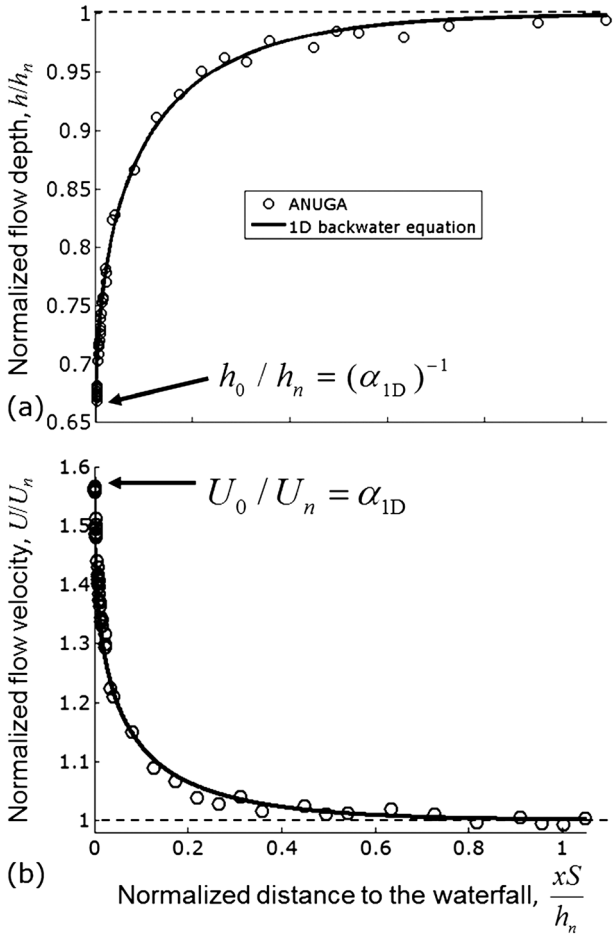

Figure 2. (a) Depth and (b) velocity profiles approaching a waterfall composed of a 1-D linear step for subcritical flow (at $xS/h_n = 0$, where x is the streamwise distance as measured from the waterfall and S is the bed slope). The solid black line (analytical 1-D backwater solution, equation (6)) and the solid circles (as modeled from ANUGA, an implementation of the 2-D depth-averaged shallow-water equations) match and converge toward the normal flow depth and velocity at a backwater length ($x \approx L_b \approx h_n/S$) upstream of the waterfall. Dashed lines respectively indicate normal flow depth and velocity.

upstream, where flow is not affected by the presence of the waterfall) [*Chow*, 1959]. Thus, $\alpha_{1D} > 1$ implies faster flow at the waterfall brink due to spatial acceleration.

Natural horseshoe waterfalls and many engineering structures depart from a purely one-dimensional linear step, and flow velocities at the waterfall brink and discharge into canyon head likely differ significantly from the 1-D case. In specific applications, waterfall geometry has been accounted for using sophisticated 3-D flow simulations [e.g., *Feurich et al.*, 2011]. However, no study has systematically investigated how flow acceleration, discharge into the canyon head, and lateral flow focusing are affected by waterfall planform geometry across a wide range of canyon sizes, flood sizes, and Froude numbers.

We aim to test the hypotheses that the horseshoe geometry of waterfalls results in flow accelerations that differ from the 1-D case and that flow discharge per unit width into the canyon head is increased owing to lateral flow focusing. To do this, we performed a series of numerical experiments. In section 2, we describe our modeling objectives, identify potential controls on flow focusing upstream of horseshoe waterfalls, and explain our modeling strategy. In section 3, we describe the numerical model ANUGA [*Roberts et al.*, 2008, 2009] which is used to investigate focusing of floods into canyons of different sizes. In section 4, we synthesize results of the experiments. In section 5, we develop semiempirical functional relationships for flow acceleration and cumulative head discharge. Last, we discuss application to engineered horseshoe spillways and controls on waterfall formation and shape.

2. Modeling Objectives

Our modeling goal is to systematically evaluate the cumulative discharge and flow acceleration factor around the brink of 2-D horseshoe waterfalls as a function of canyon width, length, upstream bed slope, flood width, flood discharge, and normal flow Froude number. In particular, we seek a generic relationship for the flow acceleration factor and flow discharge for 2-D waterfalls. To accomplish our goal, in this section, we define quantitative metrics that will be used to define the effects of 2-D flow focusing. Next, we use dimensional analysis to formulate quantitative hypotheses for the functional relationships between these metrics and the relevant topographic and hydraulic parameters. Finally, we describe the modeling strategy and parameter space covered.

2.1. Two-Dimensional Flow Focusing Metrics

In 1-D open-channel flow with constant channel width, the volumetric water discharge per unit width ($q = Uh$, where h is flow depth) is conserved such that the discharge over the waterfall ($q_0 = U_0 h_0$) is equal to the

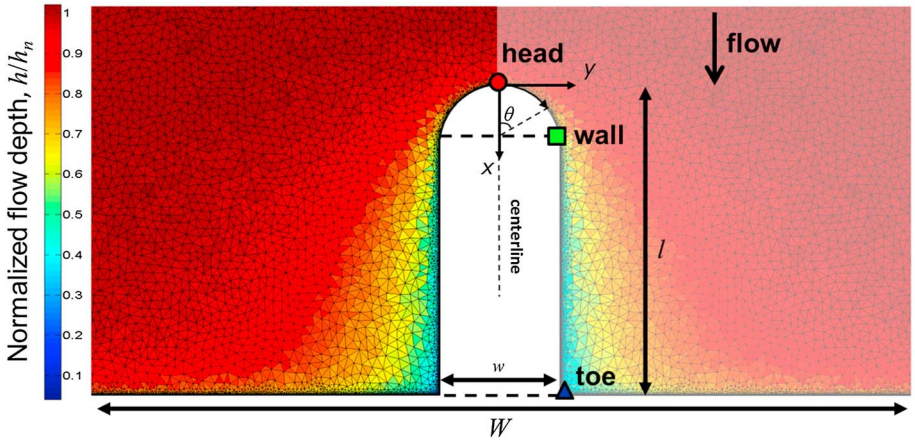

Figure 3. Plan view geometry of a flood (width *W*) flowing downslope (*S*) toward a canyon (width *w*, length *l*). The head is semicircular of radius *w*/2. The unstructured triangular mesh used in the model refines at the canyon brink to a resolution of $4 \times 10^{-3} L_b$, where L_b is the backwater length (equation (7)). The red circle, green square, and blue triangle show the locations of where we measure the acceleration factor at the head (α^*_h), the head-to-wall junction (α^*_w), and the toe (α^*_t), respectively. The angle θ is the azimuth as measured between the canyon centerline and any point around the canyon head. Color coded is an example of flow depths normalized by the normal flow depth of the flood.

normal flow discharge upstream ($q_n = U_n h_n$), and therefore, $\alpha_{1D} = U_0/U_n = h_n/h_0$ (Figure 2), where h_n is the normal flow depth and h_0 is the flow depth at the waterfall brink. The acceleration factor in 1-D was found to be well approximated by [*Rouse*, 1936; *Hager*, 1983]

$$\alpha_{1D} \equiv \frac{U_0}{U_n} = \begin{cases} \dfrac{1+\varepsilon}{\mathrm{Fr}_n^{2/3}}, & \text{if } \mathrm{Fr}_n < 1 \\ \dfrac{\mathrm{Fr}_n^2 + \varepsilon}{\mathrm{Fr}_n^2}, & \text{if } \mathrm{Fr}_n \geq 1 \end{cases} \tag{1}$$

where $\varepsilon \approx 0.4$ is an empirical constant that accounts for the deviation of pressure from hydrostatic at the waterfall brink and $\mathrm{Fr}_n = U_n/\sqrt{gh_n}$ is the normal flow Froude number. For subcritical flows ($\mathrm{Fr}_n < 1$), equation (1) results in a Froude number at the waterfall brink, Fr_0, of about 1.66 (i.e., $\mathrm{Fr}_0 = \alpha_{1D}{}^{3/2}\mathrm{Fr}_n = (1+\varepsilon)^{3/2} \approx 1.66$) regardless of the upstream Froude number (Fr_n). For supercritical flow upstream of the waterfall ($\mathrm{Fr}_n > 1$), equation (1) results in an acceleration factor that approaches unity (i.e., $\mathrm{Fr}_0 \approx \mathrm{Fr}_n$) as Fr_n increases.

Natural waterfall geometries can be complex. Because our goal is to study 2-D flow focusing as generically as possible, and because an analysis of this sort has not been conducted before, here we start with a simple geometric representation of waterfalls that remains faithful to the horseshoe shape typical of many waterfalls, canyon heads, and engineered structures (Figure 3). We consider a canyon of spatially uniform width *w* (measured in the *y*, or cross-slope, direction) and length *l* (measured in the *x*, or downslope, direction) that has a semicircular head of radius *w*/2. Downslope and cross-slope are directions defined by a fixed-Cartesian coordinate system, in which the *x* axis follows the topographic slope at a constant gradient *S*, and thus the normal flow direction (Figure 3). Downstream and cross-stream refer to directions along or perpendicular to a streamline and thus may deviate from the *x* and *y* directions due to flow focusing. A sheet flood of width *W* is centered about the canyon and has a constant discharge per unit width q_n far upstream of the waterfall, where flow depth is equal to the normal flow depth h_n. There is no bed slope in the *y* direction, such that any flow convergence toward the canyon is purely hydrodynamic. The drop height is sufficiently large such that the flow upstream of the knickpoint is not affected by flow in the plunge pool [e.g., *Bennett*, 1999; *Bennett and Casali*, 2001].

To quantify 2-D flow focusing, we define a local two-dimensional flow acceleration factor $\alpha_{2D} \equiv U_p/U_n$, which is analogous to the acceleration factor in 1-D, except that here U_p is defined in the direction

perpendicular to the local canyon brink (because it is this component only that will contribute to discharge into the canyon head), such that α_{2D} is a local quantity that is likely to vary at different locations along the waterfall brink. To highlight truly 2-D effects, throughout this paper, we will use an acceleration factor ratio α^*, defined as

$$\alpha^* \equiv \frac{\alpha_{2D}}{\alpha_{1D}} \tag{2}$$

such that $\alpha^* = 1$ corresponds to scenarios that show only 1-D flow acceleration.

To quantify changes in discharge to the waterfall as a result of lateral flow focusing, we define the local discharge per unit width as $q_0 = U_p h$. The total discharge entering the semicircular canyon head is then $Q_h = \int_{\theta=-\pi/2}^{\pi/2} q_0(\theta)\frac{w}{2}d\theta$, where θ is the azimuth with respect to the canyon centerline. The normalized cumulative head discharge q^* is defined as the ratio of Q_h to Q_n, in which $Q_n = q_n w$ is the normal flow discharge flowing across a length w, that is,

$$q^* \equiv \frac{Q_h}{Q_n} = \frac{1}{q_n}\int_{\theta=0}^{\pi/2} q_0(\theta)d\theta \tag{3}$$

A normalized cumulative head discharge of unity ($q^* = 1$) corresponds to the case where no lateral flow focusing is observed.

2.2. Dimensional Analysis and Hypotheses

To identify the controlling variables on flow acceleration (α^*) and normalized cumulative flow discharge (q^*), we use dimensional analysis for flow acceleration at steady state. Consequently, the flow variables (velocities and depth) around the canyon are time independent and fully determined by seven dimensional variables: inflow discharge per unit width q_n, acceleration of gravity g, normal flow depth h_n, canyon width w, flood width W, canyon length l, and bed slope S. This problem can be recast in terms of five dimensionless parameters,

$$(\alpha^*, q^*) = f(\mathrm{Fr}_n, w^*, W^*, l^*, S) \tag{4}$$

where $w^* = \frac{w}{W}$ is the canyon width to flood width ratio, $W^* = \frac{(W-w)S}{2h_n}$ is herein called the flood width limitation factor, and $l^* = \frac{lS}{h_n}$ is herein called the downslope backwater factor (Figure 4). The normal flow depth can be defined as $h_n = \frac{C_f U_n^2}{gS}$, where $C_f = \frac{U_n^2}{u_*^2}$ is a bed friction coefficient and u_* is the bed shear velocity [e.g., *Chow*, 1959].

Dimensional analysis does not dictate which dimensionless numbers are best suited to describe the physics of flow focusing. In the rest of this section, we describe why the dimensionless numbers we picked make intuitive sense and are likely relevant to flow focusing upstream of canyons.

The normal flow Froude number $\left(\mathrm{Fr}_n = U_n/\sqrt{gh_n}\right)$ describes the ratio of downstream oriented, normal flow velocity to the shallow-water-wave speed. For $\mathrm{Fr}_n < 1$, the velocity of shallow-water waves $\left(\sqrt{gh_n}\right)$ is greater than the flow velocity (U_n), and thus, waves can propagate in all directions. For $\mathrm{Fr}_n > 1$, the velocity of waves is smaller than that of the flow, and waves can only propagate downstream and cross-stream. Consequently, the Froude number sets the direction and distance at which hydraulic information propagates and is thus expected to exert a major control on the degree to which water is focused toward the canyon head.

The waterfall width relative to the flood width (w^*) is important because it governs the proportion of water available to be focused into the canyon. Figure 4 shows that narrow floods ($w^* \approx 1$) will result in a canyon that is mostly a horseshoe without sidewalls because of the fixed semicircular geometry of the head, at constant l^* and W^*. When $w^* \ll 1$, the canyon sidewalls make up most of the canyon length, and we expect that w^* ceases to be an important parameter.

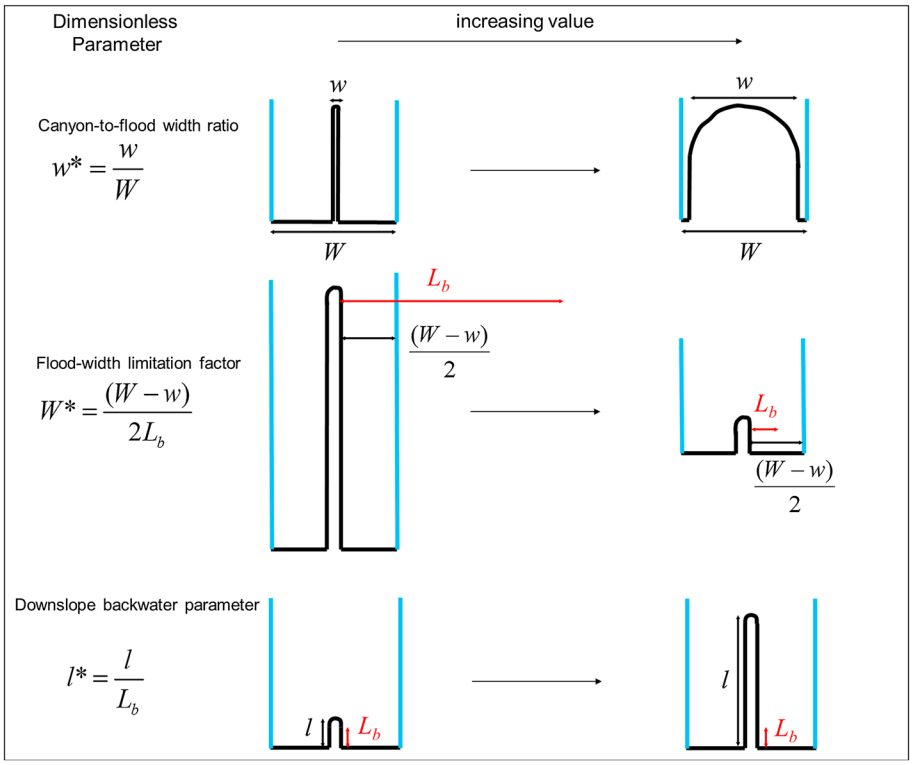

Figure 4. Conceptual plan view cartoons of floods flowing over canyon escarpments to illustrate the dimensionless parameters w^*, W^*, and l^*. Blue lines delineate the flood width, while black lines delineate the waterfall brink. Red arrows represent the backwater length scale L_b. The black arrows pointing to the right indicate that a given dimensionless parameter is increased while all others are held constant. The other two independent dimensionless parameters, Fr_n and S, are not shown.

The lateral backwater limitation factor (W^*) is the ratio of the half flood width $(W - w)/2$, measured from the canyon sidewalls, to the backwater length scale $L_b = \frac{h_n}{S}$. The backwater length is a typical length scale over which 1-D open-channel flows are affected by downstream boundary conditions [e.g., *Chow*, 1959]. Here we wish to describe cross-slope backwater dynamics (i.e., lateral flow focusing); thus, C_f may be the more relevant scale (rather than S) in determining a characteristic backwater length. This notwithstanding, for normal flow, $\mathrm{Fr}_n = U_n/\sqrt{gh_n} = \sqrt{S/C_f}$, and therefore S and C_f can be used interchangeably if Fr_n is an independent parameter. Consequently, $W^* > 1$ indicates that the half flooded width from the canyon sidewalls is larger than the lateral backwater length (Figure 4) and thus that hydraulics at the canyon sidewalls will not be affected by lateral backwater limitations due to the domain width. On the contrary, when $W^* < 1$, half of the flooded width is smaller than the lateral backwater length (Figure 4), and we expect hydraulics at the canyon sidewalls will be affected by the boundaries of the flood, leading to decreased α^* and q^*. With all other nondimensional parameters held constant, increasing W^* also results in canyons that are shorter with respect to the flood width if w^* and l^* are held constant (Figure 4). When a canyon widens, w^* increases and W^* decreases such that both effects may act in concert to decrease α^* and q^* at the canyon sidewalls.

We expect that the downslope backwater factor (l^*) also controls the degree of drying along the canyon sidewalls. Longer canyons with higher l^* should capture more of the flood water at the canyon head or shortly downslope, potentially leaving canyon sidewalls downslope of the canyon head dry. Figure 4 shows how canyon length and L_b vary for different values of l^*.

Finally, we found that model simulations are exactly equivalent for different bed slopes ($5 \times 10^{-4} < S < 5 \times 10^{-2}$) if Fr_n and W^* are held constant. That is, bed slope has no effect on flow focusing independent of its role in determining the Froude number and the lateral backwater length scale. Consequently, the number of independent variables in equation (4) is simplified from five to four.

Table 1. Dimensionless and Dimensional Parameter Ranges Encompassed by the Simulations

		Number of Simulations	Dimensionless Variables					Dimensional Parameters					
			$Fr_n = \frac{U_n}{\sqrt{gh_n}}$	$w^* = \frac{w}{W}$	$W^* = \frac{(W-w)S}{2h_n}$	$l^* = \frac{lS}{h_n}$	S	w (m)	W (m)	l (m)	q_n (m^2/s)	n (s/m$^{1/3}$)	h_n (m)
Base cases	subcritical	1	0.5	0.1	4.5	30	0.0075	200	2,000	6,000	2.88	0.059	1.5
	supercritical	1	3	0.1	4.5	30	0.0075	200	2,000	6,000	17.26	0.0099	1.5
Experiment series 1: Froude number, Fr_n		9	0.4–5	0.1	4.5	30	0.0075	200	2,000	6,000	2.30–28.77	0.074–0.006	1.5
Experiment series 2: Canyon width to flood width ratio, w^*		12	0.5, 3	0.1–0.9	4.5	30	0.0075	200–2,595	2,000–3,000	1,000–6,000	0.31–17.26	0.007–0.06	0.25–1.5
Experiment series 3: Lateral backwater limitation factor, W^*		14	0.5, 3	0.1	0.125–15	30	0.0075	1.5–112	15–1,120	1,620–6,395	0.4–19.0	0.009–0.06	0.41–1.6
Experiment series 4: Downslope backwater parameter, l^*		22	0.5, 3	0.1	4.5	0.55–30	0.0075	200	2,000	110–4,000	2.88	0.059	1.5
Test simulations		45	0.5–1.3	0.1–0.9	0.02–4.5	0.55–30	5×10^{-4}–5×10^{-2}	137.14–13,714	480–48,000	200–51,429	2.88–472.74	0.02–0.10	1.5–45

2.3. Modeling Strategy and Parameter Space

We performed a series of numerical experiments to test our hypotheses and to find functional relationships for equation (4). We systematically varied one of the four dimensionless parameters (experiment series 1 to 4), while all the others were set constant (Table 1), and extracted the acceleration factors (normalized by their 1-D counterpart α_{1D}) at the center of the canyon head ($\alpha^*_h = \alpha^*(\theta = 0)$, red circle in Figure 3), at the most upstream node of the sidewall ($\alpha^*_w = \alpha^*(\theta = \pi/2)$, green square in Figure 3), and at the toe of the canyon where it joins the downslope escarpment ($\alpha^*_t = \alpha^*$ at the downslope end of the canyon, blue triangle in Figure 3). We picked these three locations as representative of different canyon segments that are important for understanding canyon widening (e.g., erosion at the canyon head versus sidewall) and canyon lengthening (e.g., erosion at the canyon head versus toe), where erosion rate is likely a function of flow velocity. Note that the acceleration factor ratio at the toe α^*_t could be measured in both the downslope and cross-slope directions. We chose to report its values in the downslope (x) direction because this is the direction that allows for a comparison between the dynamics of the canyon head and of the escarpment at the base of the canyon.

Two numerical simulations are common to experiment series 1 to 4, one subcritical ($Fr_n = 0.5$) and one supercritical ($Fr_n = 3$). We refer to these simulations as the base cases. The base cases simulate a low-sloping ($S = 0.0075$), wide sheet flood ($w^* = 0.1$) that has a lateral backwater length which is shorter than the half flooded width ($W^* = 4.5$) and that pours over the brink of a long canyon ($l^* = 30$). Under these conditions, we expect that mostly Froude number Fr_n will influence the distribution of acceleration factor ratios around the canyon head.

3. Numerical Methods

ANUGA is a finite-volume modeling suite that solves the two-dimensional time-dependent depth-averaged shallow-water equations on an unstructured mesh of triangular cells where friction is implemented using Manning's equation [*Zoppou and Roberts*, 1999; *Roberts et al.*, 2008, 2009; *Mungkasi and Roberts*, 2011, 2013]. The shallow-water equations describe conservation of mass and conservation of momentum, where the

forcing terms are gravity, friction, and pressure gradients. In the case of no bed slope in the y direction, the conservation equations are

$$\begin{cases} \dfrac{\partial h}{\partial t} + \dfrac{\partial (U_x h)}{\partial x} + \dfrac{\partial (U_y h)}{\partial y} = 0 \\ \dfrac{\partial (U_x h)}{\partial t} + \dfrac{\partial (U_x^2 h)}{\partial x} + \dfrac{\partial (U_x U_y h)}{\partial y} = -gh\dfrac{\partial h}{\partial x} - ghS - \dfrac{C_f U_x}{h}\sqrt{U_x^2 + U_y^2} \\ \dfrac{\partial (U_y h)}{\partial t} + \dfrac{\partial (U_x U_y h)}{\partial x} + \dfrac{\partial \left(U_y^2 h\right)}{\partial y} = -gh\dfrac{\partial h}{\partial y} - \dfrac{C_f U_y}{h}\sqrt{U_x^2 + U_y^2} \end{cases} \quad (5)$$

in which U_x and U_y are the depth-averaged velocities in the x and y directions, respectively, and C_f is related to Manning's n through $C_f = \frac{n^2 g}{h^{1/3}}$.

These equations are derived by depth averaging the Navier-Stokes equations under the slender flow approximation, which assumes that the vertical length scale is negligible compared to the horizontal. A consequence of this assumption is that vertical pressure gradients are hydrostatic. The model implementation is capable of reproducing wetting and drying, flow around structures, and hydraulic jumps due to the ability of the upwind central scheme to accommodate discontinuities in the solution [*Kurganov et al.*, 2001].

Theoretically, the slender flow approximation does not hold at the waterfall brink because there pressure is not hydrostatic. It was shown that the distance upstream of a waterfall at which pressure becomes hydrostatic is about one to two critical depths h_c (i.e., the depth in which Fr = 1; for the 1-D case, $h_c = \left(q_n^2/g\right)^{1/3}$) [*Hager*, 1983], which implies that the region that violates the shallow-water equations is limited to very near the waterfall brink. Indeed, ANUGA has been successfully tested against dam break experiments [*Nielsen et al.*, 2005] and was able to reproduce with great accuracy water surfaces and bed shear stress [*Barnes and Baldock*, 2006; *Mungkasi and Roberts*, 2013].

Despite that nonhydrostatic pressure at the brink is not accounted for in our modeling, its effect can be incorporated by assuming that the same nonhydrostatic pressure captured in the 1-D acceleration factor (equation (1)) holds for 2-D canyons. This approximation is likely to be true given that (1) the boundary condition on pressure is the same all around the canyon brink—pressure at the waterfall is atmospheric and (2) the length scale over which nonhydrostatic effects are important (a few critical depths) is much smaller than the radius of curvature of most horseshoe waterfalls, such that enhanced flow acceleration due to 2-D nonhydrostatic effects in such close proximity to the waterfall brink is unlikely to be significant in the cross-stream direction. As a result, we expect the acceleration factor ratio α^* to be unchanged by nonhydrostatic effects, and it is therefore possible to calculate the acceleration for a 2-D waterfall using our relationships for α^*, combined with equation (1) that accounts for nonhydrostatic effects in 1-D.

We also tested ANUGA against the solution to the one-dimensional backwater equation [e.g., *Chow*, 1959] for subcritical flows (Figure 2) by solving

$$\frac{dh}{dx} = \frac{S - C_f\,\mathrm{Fr}^2}{1 - \mathrm{Fr}^2} \quad (6)$$

Like ANUGA, equation (6) also employs the slender flow approximation and does not capture nonhydrostatic effects at the brink. The solution to equation (6) was computed with a predictor-corrector, central scheme finite difference code [e.g., *Butcher*, 2008]. In the 1-D model, we set $\mathrm{Fr}_n = 0.99$ at the downstream boundary to simulate the water surface drawdown at the waterfall. In ANUGA, we extracted flow depths along a line at the edge of a wide flood. Figure 2 shows that ANUGA is able to reproduce with good accuracy the water depth and velocity for 1-D flow toward a waterfall with no lateral flow focusing.

The user-defined parameters for ANUGA are (1) the mesh (topography and spatially variable resolution), (2) initial and boundary conditions, (3) Manning's n, and (4) duration of the simulation, which are described below. Time step intervals are internally determined from spatial resolution to enforce stability of the solution.

3.1. Domain Geometry and Resolution

We model the same canyon and flood system as described in section 2. The numerical domain was set to optimize computational time. We only model half of the domain, because it is symmetric with respect to the canyon axis. Depth and velocity gradients get steeper toward the brink (Figure 2). In order to capture these steep gradients and better resolve the acceleration factor at the brink, we defined the cliff as a set of three parallel lines, one downstream of the brink, one making up the brink, and one upstream of the brink. This setup allows us to extract flow variables along a line that runs parallel to the brink but is slightly upstream of it and thus not affected by numerical noise induced by the near-vertical step at the brink. For subcritical input flows, these lines are separated by a small distance of $4\times10^{-3}L_b$ along the plane of the bed. To estimate L_b, we used the analytical solution for subcritical flows in rectangular 1-D channels [*Bresse*, 1860],

$$L_b = \lim_{r\to 1}\left\{\frac{h_n}{S}\left[r - \frac{h_c}{h_n} - \left(1-\mathrm{Fr}_n^2\right)\left(\Gamma(r) - \Gamma\left(\frac{h_c}{h_n}\right)\right)\right]\right\} \tag{7}$$

where $\Gamma(r) = \frac{1}{6}\ln\left(\frac{r^2+r+1}{(r-1)^2}\right) - \frac{1}{\sqrt{3}}\arctan\left(\frac{\sqrt{3}}{2r+1}\right)$ and $r = \frac{h(x=L_b)}{h_n} = 0.95$ is the assumed ratio of flow depths at the backwater extent [e.g., *Lamb et al.*, 2012]. For supercritical flows, we set the distance between the lines that define the cliff to be $4\times10^{-3}h_c/S$. Outside of these lines, the resolution of the unstructured triangular mesh is about 25 times the brink resolution, which allows for a less dense sampling of flow variables where spatial gradients are less steep.

3.2. Initial and Boundary Conditions

The domain length upstream of the canyon head is set to L_b for subcritical floods and h_c/S for supercritical floods. This ensures that the flow depth at the inflow boundary is equal to the normal flow depth and thus that brink vertices are not affected by the inflow boundary. The inflow boundary is set as a Dirichlet condition on stage and momenta, where stage is set to the normal flow depth, the downslope momentum is set to the desired discharge per unit width q_n, and the cross-slope momentum is set to zero. The side boundaries are reflective and frictionless, such that there is no flow across the edge of the domain. Finally, the downstream boundary condition is located a few vertices downstream of the cliff and is fully transmissive, that is, all flow is transmitted outside of the domain. The drop height is set to 10 critical depths. The initial depth is set to the normal flow depth h_n everywhere, and the model is run in time until steady state is reached. We detect steady state by computing the quadratic residual in flow depth between consecutive time steps. When this residual becomes smaller than a threshold of 0.1%, the experiment is stopped.

The error bars on flow depths and velocities induced by instabilities at the brink are at most of 0.5% and 2% of the mean respectively as estimated from the variability of flow depth and velocity around the brink at 100 consecutive time steps. Error bars associated with numerical variability are smaller than symbol sizes in all figures of the paper.

4. Results

4.1. Base Cases

The two base case simulations (see Table 1 for parameter values) correspond to the case where the canyon head is not affected by the edges of the flood ($w^* \ll 1$ and $W^* > 1$) or the length of the canyon ($l^* \gg 1$), that is, they correspond to a sheet flood.

Figures 5a and 5b show the distribution of normalized discharge per unit width $(Uh)/q_n$ in plan view for the subcritical and supercritical base cases, respectively. Black lines with arrows follow streamlines, that is, the trajectories of flow particles within the flood. In both base cases, discharge per unit width is slightly enhanced around the canyon head (i.e., $(Uh)/q_n \geq 1$) and is progressively depleted as water flows downslope toward the canyon toe (i.e., $(Uh)/q_n < 1$). The relative decrease in discharge per unit width compared to the normal flow discharge per unit width is caused by the loss of water into the canyon further upslope. The cross-slope extent of the relative decrease in discharge per unit width is larger in the subcritical base case than in the supercritical base case and correlates with the plan view curvature of the

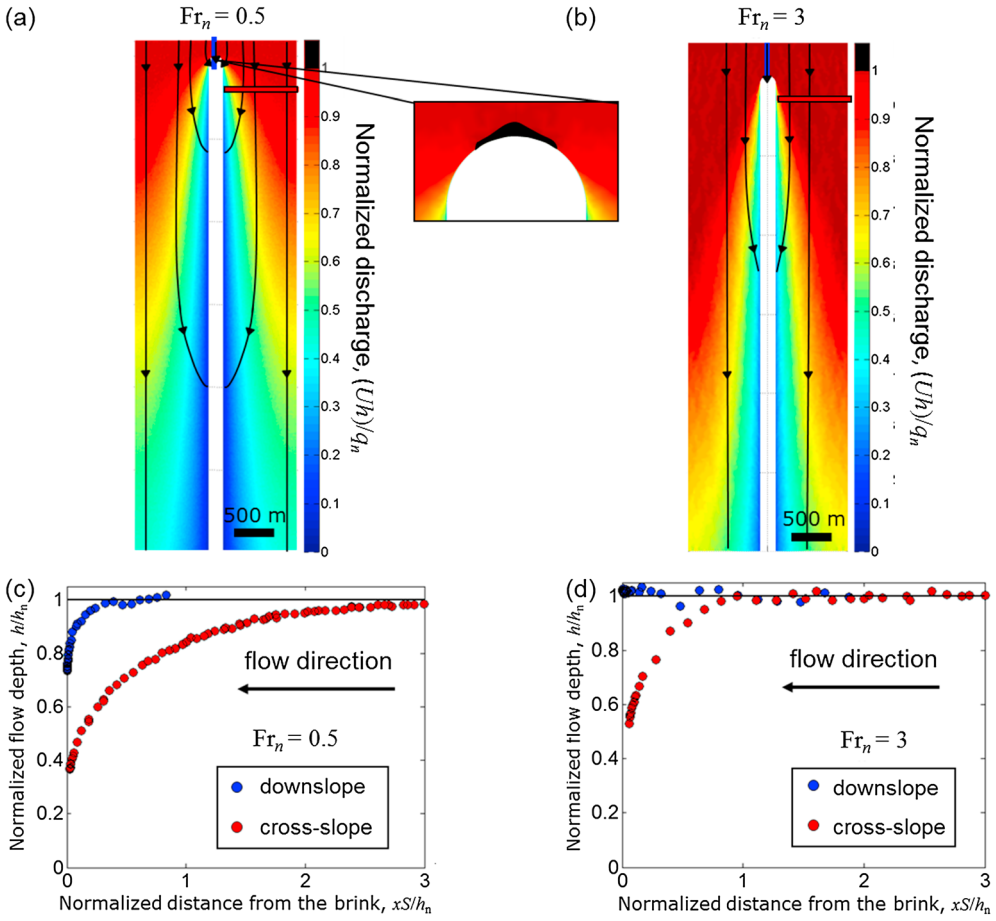

Figure 5. Normalized discharge map for the (a) subcritical ($Fr_n = 0.5$, $w^* = 0.1$, $W^* = 4.5$, $l^* = 30$, $S = 0.0075$) and (b) supercritical ($Fr_n = 3$, $w^* = 0.1$, $W^* = 4.5$, $l^* = 30$, $S = 0.0075$) base runs. Black lines with arrows show streamline directions. U is the magnitude of flow velocity such that $U = \sqrt{U_x^2 + U_y^2}$. Inset in Figure 5a shows the zone around the canyon head where discharge per unit width is enhanced from the 1-D case $\left(\text{i.e., } \frac{Uh}{q_n} \geq 1\right)$ highlighted in black. Discharge per unit width is not enhanced around the head for supercritical floods. Normalized depth profiles for the same (c) subcritical and (d) supercritical base runs. The profiles were measured along the canyon centerline (blue line in Figures 5a and 5b, blue symbols in Figures 5c and 5d) and along a cross-slope profile (red line in Figures 5a and 5b, red symbols in Figures 5c and 5d).

streamlines. In the subcritical case, streamlines strongly deviate from pure downslope trajectories, and a significant amount of water is focused into the canyon, which leads to a large decrease in normalized discharge per unit width downslope. In the supercritical case, streamlines only deviate from pure downslope trajectories close to the canyon walls, which leads to less focusing of water into the canyon, and thus a lower decrease in normalized discharge per unit width downslope.

Figures 5c and 5d show normalized flow depth profiles along downslope (blue) and cross-slope (red) transects for both base cases as located by the blue and red lines in Figures 5a and 5b. In the subcritical case, water depth is equal to normal flow depth far from the waterfall brink in both profiles. Along the downslope profile, water depth is drawn down to the critical depth h_c at the waterfall due to spatial acceleration of water toward the brink. The length scale over which water is drawn down scales with the backwater length $L_b \propto h_n/S$ (equation (7)). Along the cross-slope profile, water depth is also drawn down toward the waterfall brink, but over a longer spatial scale because there is no cross-slope topographic gradient. In the supercritical case, the normal flow and critical depths are equal (i.e., $h_n = h_c$); that is, there is no drawdown effect in the downslope direction. Nevertheless, a backwater profile develops in the cross-slope direction, because cross-slope flow is subcritical, which results in the plan view curvature of the streamlines in Figure 5b.

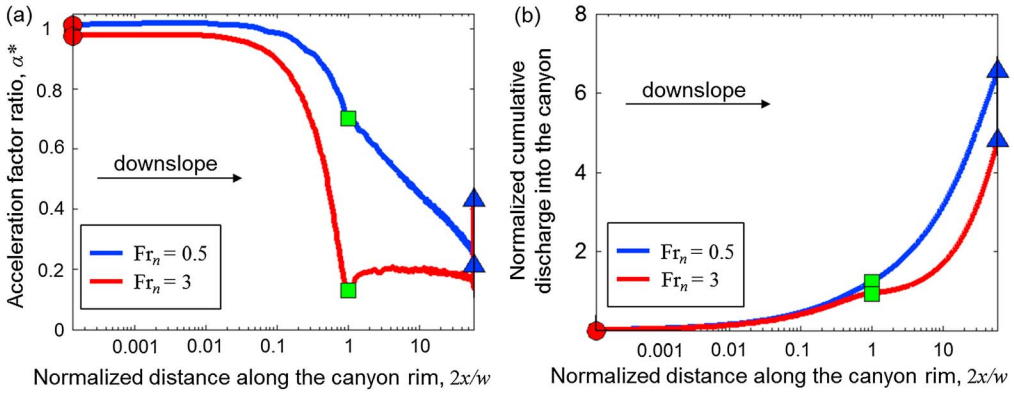

Figure 6. (a) Acceleration factor ratio α^* and (b) normalized cumulative discharge along the rim of the canyon for the base runs. The abscissa is the distance measured along the spatial x axis (Figure 3) from the center of the canyon head, normalized by $w/2$, such that this distance equals unity at the head-to-wall junction (i.e., where $\theta = \pi/2$). The normalized cumulative head discharge q^* is thus found where $2x/w$ equals unity. Red circles indicate the canyon head center, green squares the head-to-wall junction, and blue triangles the canyon toe (Figure 3). Note that the acceleration factor at the toe (blue triangle) is measured in the downslope (x) direction and hence is offset from the profile that shows acceleration in cross-slope (y) direction at the corner junction between the canyon and the escarpment.

Figures 6a and 6b respectively show the acceleration factor ratio α^* and normalized cumulative discharge into the canyon as a function of normalized distance along the canyon rim for the subcritical (blue) and supercritical (red) base cases. Both quantities are measured in the direction perpendicular to the brink. The distance along the canyon rim is projected along the canyon centerline, so that a normalized distance along the canyon rim of zero corresponds to the location of the tip of the canyon head (red circle in Figure 3), while a value of unity corresponds to the location of the canyon wall (green square in Figure 3). Consequently, the value of the cumulative head discharge q^* is found by reading the value of the normalized cumulative discharge into the canyon at an x axis value of unity. The last measured acceleration factor ratios and normalized cumulative discharges correspond to the location of the canyon toe (blue triangle in Figure 3). Note that the value of the acceleration factor ratio at the toe is discontinuous because it is measured in the cross-slope direction along the sidewalls, and in the downslope direction from the toe along the escarpment at the base of the canyon.

Figure 6a shows that at $\mathrm{Fr}_n = 0.5$, the velocity perpendicular to the brink progressively decreases along the canyon rim from the center of the canyon head to the canyon sidewall because water is lost into the canyon due to flow focusing. At $\mathrm{Fr}_n = 3$, the change in velocity along the canyon rim is more pronounced due to higher momentum flow and less focusing of water into the canyon. Along the canyon sidewall, the cross-slope velocity is constant and very small because water is not efficiently focused into the canyon. Figure 6b shows that the cumulative discharge into the canyon is greater at $\mathrm{Fr}_n = 0.5$ than at $\mathrm{Fr}_n = 3$, again because water is more efficiently deflected toward the canyon head for subcritical flows, such that $q^* > 1$ in the subcritical case, while $q^* \approx 1$ in the supercritical case. Moreover, discharge is significantly larger in the cross-slope direction along the canyon walls in the subcritical case than in the supercritical case. Nevertheless, flow focusing for supercritical normal flow is still finite because cross-slope Froude numbers are subcritical.

In summary, subcritical normal flow leads to the development of both downslope and cross-slope backwater profiles, which deflects streamlines and enhances flow focusing, α^* and q^*. In contrast, there is no downslope backwater profile for supercritical normal flow, and only cross-slope backwater profiles contribute to spatial acceleration of water.

4.2. Experiment Series 1: Froude Number Fr_n

Experiment series 1 was designed to investigate sheet floods of varying Froude number Fr_n. We varied Froude number from 0.4 to 5 (Table 1) and used $w^* = 0.1$, $W^* = 4.5$, $l^* = 30$, and $S = 0.0075$ (as in the base cases). This range of Froude numbers is typical of large-scale floods [*Costa*, 1987]. These floods are much wider than the canyon width, and the canyons are long.

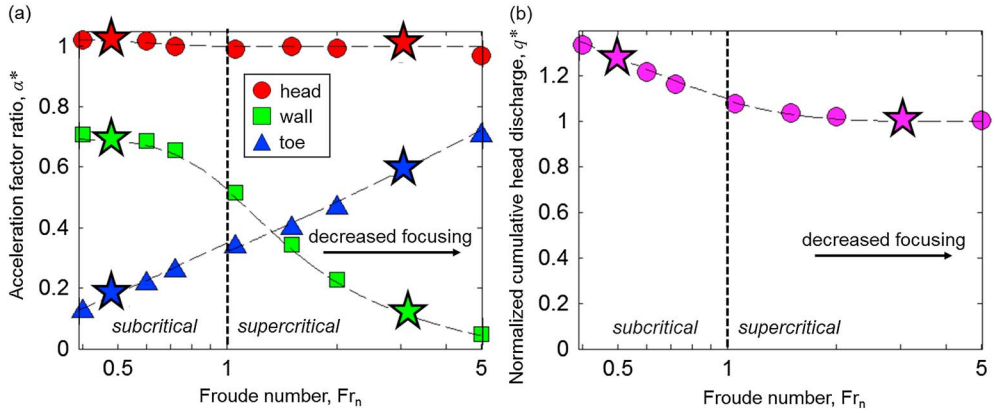

Figure 7. (a) Acceleration factor ratio α^* and (b) normalized cumulative head discharge q^* as a function of normal flow Froude number Fr_n. The other parameters were held constant ($w^* = 0.1$, $W^* = 4.5$, $l^* = 30$, $S = 0.0075$). Figure 7a shows the acceleration factor ratios along the brink of the canyon at the centerline of the head, junction of the head and sidewalls ("wall"), and junction between the canyon sidewall and the base of the escarpment ("toe") (Figure 3). The stars represent the subcritical ($Fr_n = 0.5$) and supercritical ($Fr_n = 3$) base runs. Thin dashed lines are the best fit solutions discussed in section 5.

In Figure 7, we show the value of α^* at three locations along the canyon brink—the center of the canyon head, the junction between the canyon head and the sidewall, and the junction between the canyon sidewall and the downstream escarpment (i.e., the canyon toe) (Figure 3). The acceleration factor at the canyon head is roughly equal to the 1-D acceleration factor (i.e., $\alpha_h^* \approx 1$), with a small enhancement of acceleration at lower Froude numbers (Figure 7a). For example, $\alpha_h^* = 1.03$ at $Fr_n = 0.4$. The acceleration factor at the wall is smaller than at the head $\left(\alpha_w^* < 1\right)$, but it is still significant for low Fr_n and decreases to near zero at high Froude numbers. Note that for a 1-D step, there is no cross-slope acceleration (i.e., $\alpha_w^* = 0$). The acceleration factor ratio at the toe α_t^* is lower than that at the wall (Figure 7a) and increases with Froude number. Flow focusing results in an enhancement of discharge to the canyon head of up to 34% for subcritical flows. The cumulative discharge over the waterfall head q^* decreases and eventually reaches unity as the upstream Froude number is increased (Figure 7b).

We interpret these trends as the result of higher Froude numbers producing streamlines that are oriented nearly parallel to the bed slope, whereas at lower Froude numbers more water is focused toward the canyon (e.g., Figure 5). The cross-slope component of flow velocity decreases as Froude number is increased, decreasing the velocity perpendicular to the sidewall brink. Consequently, higher Froude numbers imply that less water is lost into the canyon and more water reaches the toe, thus increasing the acceleration factor α_t^* at the toe (e.g., Figure 5). Importantly, for critical and supercritical upstream Froude numbers $Fr_n \geq 1$, the acceleration factor ratio at the canyon sidewall is nonzero because flow in the cross-slope direction is still subcritical. Normal Froude number Fr_n must exceed ~5 for cross-slope flow into the canyon head to be negligible.

4.3. Experiment Series 2: Waterfall Width to Flood Width Ratio w^*

In experiment series 2, we varied the canyon width to flood width ratio w^* from 0.1 to 0.9 for two different Froude numbers ($Fr_n = 0.5$ and $Fr_n = 3$), with all other parameters held to the base case values ($W^* = 4.5$, $l^* = 30$, and $S = 0.0075$, Table 1). By definition, w^* can only vary between zero (no canyon) and unity (fully channelized canyon). We expect that wider canyons will have decreased acceleration at their walls due to the increased amount of water lost to the head. As canyons widen while keeping a constant length, the horseshoe head progressively occupies a larger portion of the flood width, but also of the total canyon length (Figure 4). The latter effect is a direct consequence of the assumption that the canyon head is semicircular.

For subcritical floods, the acceleration factor ratio is not affected by w^* around the canyon head, but it is lower along the walls and decreases to zero at the toe (drying) as w^* increases (Figures 8a and 9a). This decrease results from a geometric effect—as w^* increases, the horseshoe head occupies more of the total flood width and captures an increasing amount of water. In the end member case of a semicircular canyon ($w^* = 1$), the wall and the toe are at the same location, the flooded width adjacent to the wall/toe is zero, and we thus expect the acceleration there to drop to zero in the cross-slope direction.

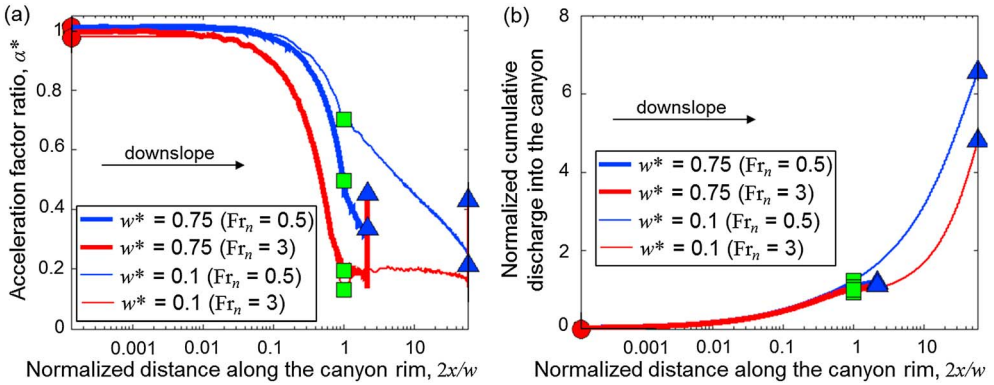

Figure 8. (a) Acceleration factor ratio α^* and (b) normalized cumulative discharge along the brink of the canyon. The abscissa is the distance measured along the spatial x axis (Figure 3) from the center of the canyon head, normalized by $w/2$, such that this distance equals unity at the head-to-wall junction (i.e., where $\theta = \pi/2$). Blue lines are subcritical runs, whereas red lines are supercritical runs. Thinner lines correspond to the base runs (with $w^* = 0.1$, Figure 5), while thicker lines have a canyon width to flood width ratio of $w^* = 0.75$. Red circles indicate the canyon head center, green squares the head-to-wall junction, and blue triangles the canyon toe (Figure 3). Note that the acceleration factor at the toe (blue triangle) is measured in the downslope (x) direction and hence is offset from the profile that shows acceleration in cross-slope (y) direction at the corner junction between the canyon and the escarpment.

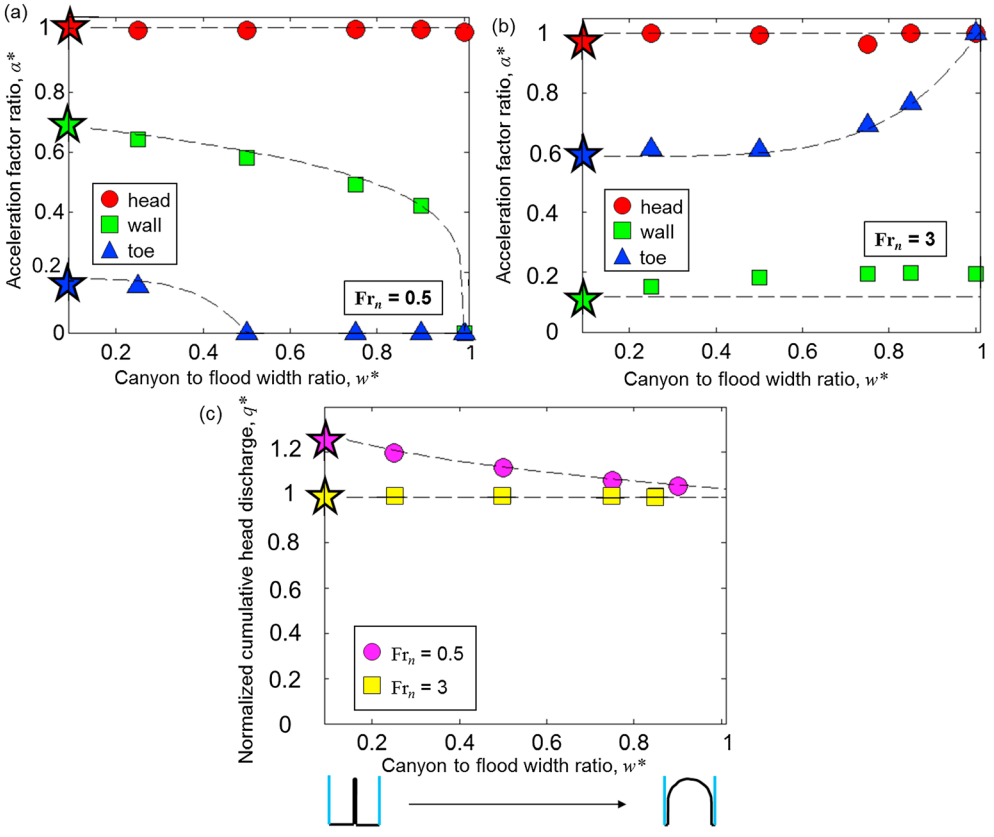

Figure 9. Acceleration factor ratio α^* as a function of the canyon width to flood width ratio w^* for (a) subcritical flows ($Fr_n = 0.5$) and (b) supercritical flows ($Fr_n = 3$). (c) Normalized cumulative head discharge q^* as a function of the canyon width to flood width ratio w^* for both subcritical ($Fr_n = 0.5$) and supercritical flows ($Fr_n = 3$). The other parameters are held constant ($W^* = 4.5$, $l^* = 30$, $S = 0.0075$). Stars represent the base case simulations. Dashed lines are the best fit solutions discussed in section 5. Sketches at the bottom of Figure 9c illustrate how plan view geometry varies as w^* increases (Figure 4).

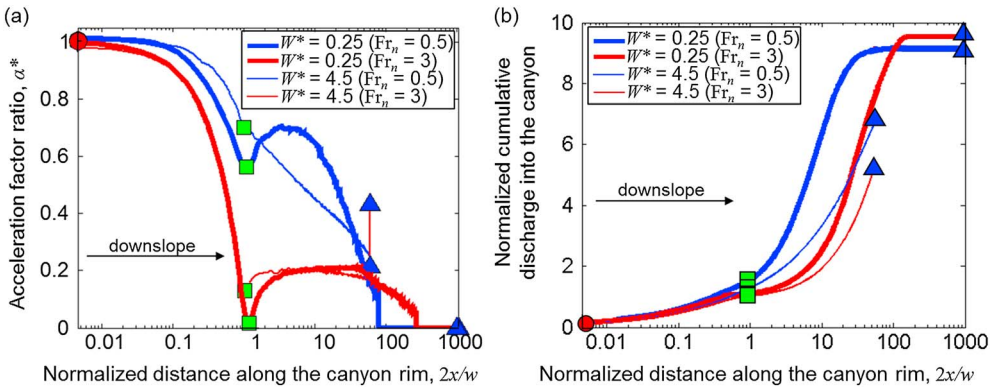

Figure 10. (a) Acceleration factor ratio α^* and (b) normalized cumulative discharge along the brink of the canyon. The abscissa is the distance measured along the spatial x axis (Figure 3) from the center of the canyon head, normalized by $w/2$, such that this distance equals unity at the head-to-wall junction (i.e., where $\theta = \pi/2$). Blue lines are subcritical runs, whereas red lines are supercritical runs. Thinner lines correspond to the base runs (with $W^* = 4.5$, Figure 5), while thicker lines have a higher lateral backwater parameter ($W^* = 0.25$). Red circles indicate the canyon head center, green squares the head-to-wall junction, and blue triangles the canyon toe (Figure 3). Note that the acceleration factor at the toe (blue triangle) is measured in the downslope (x) direction and hence is offset from the profile that shows acceleration in cross-slope (y) direction at the corner junction between the canyon and the escarpment.

For supercritical floods, the acceleration factor ratio does not vary much around the head and the wall (Figure 8a). Figure 9b shows that the acceleration factor ratio is greater at the toe than at the wall, which we interpret as the result of a decreased cross-slope component of velocity for supercritical floods (section 4.2). The acceleration factor ratio increases at the toe with increasing w^* because the canyon sidewalls are shorter and a smaller fraction of the water is lost over the brink along the sidewalls (Figure 8b).

For subcritical floods, the cumulative head discharge q^* decreases with increasing relative waterfall width (w^*), whereas q^* is constant for supercritical floods (Figures 8b and 9c). These trends correlate with the acceleration factor ratio at the wall α^*_w. In subcritical cases, an increasingly wide horseshoe head captures more of the total available water, leading to smaller flow depths near the wall, and thus decreased lateral backwater effects. In supercritical cases, flow depth does not significantly deviate from its upstream value away from the canyon wall, such that lateral backwater effects are constant as w^* increases. The cumulative head discharge q^* should plateau at unity in both subcritical and supercritical cases because all of the water enters into the head at $w^* = 1$ (Figure 9c).

4.4. Experiment Series 3: Flood Width Limitation Factor W^*

In experiment series 3, we investigated the effect of varying lateral backwater lengths for a given flood width. We thus varied the flood width limitation factor W^* from 0.12 to 15 for two different Froude numbers ($\mathrm{Fr}_n = 0.5$ and $\mathrm{Fr}_n = 3$), $w^* = 0.1$, $l^* = 30$, and $S = 0.0075$ (Table 1). Like the base cases, this corresponds to the case of a wide flood pouring over the brink of a long canyon. In theory, W^* can vary from values close to zero, when the lateral backwater length is very long compared to the flood width, to virtually infinity when the flood is very wide compared to the backwater length.

Figure 10a shows that the acceleration factor ratio decreases at the wall for lower W^*. The acceleration factor ratio at the toe decreases to zero at $W^* = 0.25$ for both subcritical and supercritical flows, indicating complete drying. Interestingly, acceleration is locally enhanced along the walls downstream of the canyon head for small W^* (Figure 10a). For this case, the canyon head radius is much smaller than the length scale over which flow convergence occurs (L_b). Thus, for $W^* \approx 0.25$, the zone of maximum flow convergence is pushed downstream of the canyon head. Overall normalized cumulative discharge into the canyon is enhanced for both subcritical and supercritical floods when W^* is large. Nevertheless, the normalized cumulative head discharge q^* is only enhanced at large W^* in the subcritical case (Figure 10b).

Figure 11a shows over a wider range in parameter space how the acceleration factor ratios at the head, wall, and toe vary as W^* increases for a subcritical flood. The acceleration factor ratio at the wall is

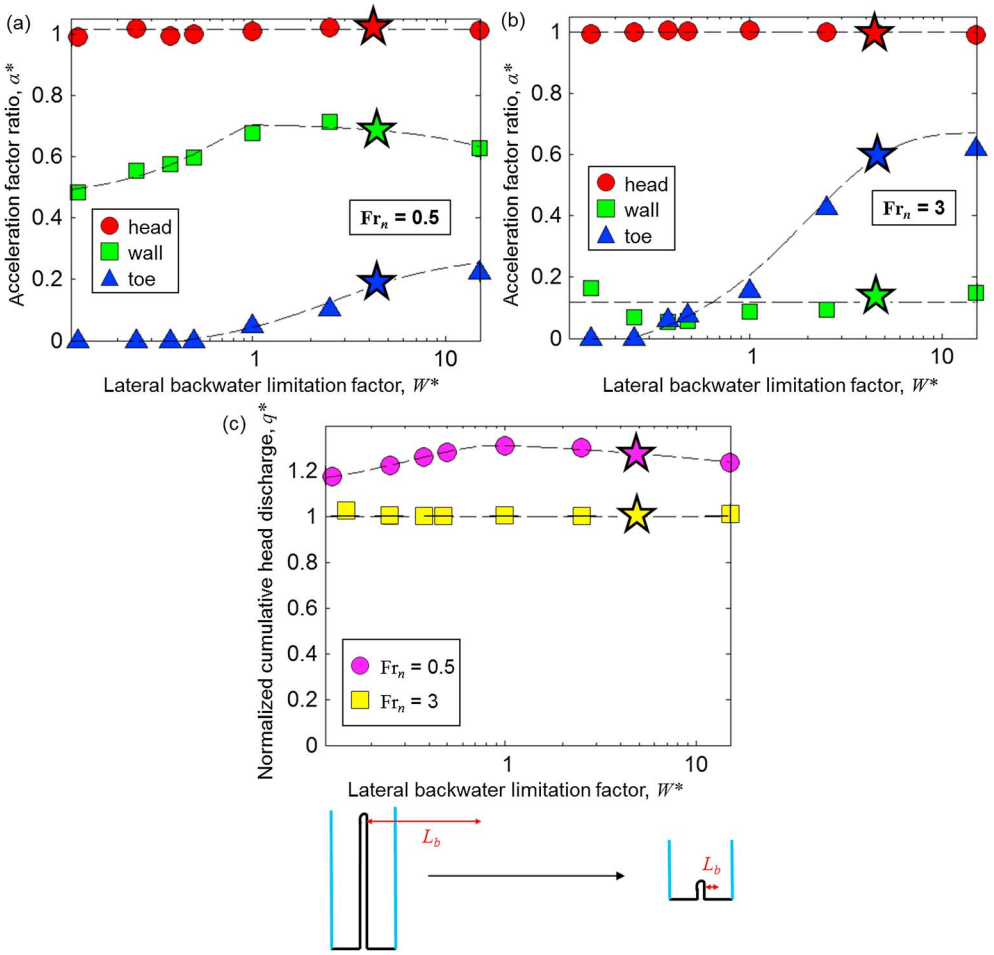

Figure 11. Acceleration factor ratio α^* as a function of the lateral backwater parameter W^* for (a) subcritical flows ($Fr_n = 0.5$) and (b) supercritical flows ($Fr_n = 3$). (c) Normalized cumulative head discharge q^* as a function of the lateral backwater parameter W^* for both subcritical ($Fr_n = 0.5$) and supercritical flows ($Fr_n = 3$). The other parameters are held constant ($w^* = 0.1$, $l^* = 30$, $S = 0.0075$). Stars represent the base case simulations. Dashed lines are the best fit solutions discussed in section 5. Sketches at the bottom of Figure 11c illustrate how plan view geometry varies as W^* increases (Figure 4).

maximum at $W^* \approx 1$. We interpret this transition at $W^* \approx 1$ as the interplay of flood width limitations ($W^* < 1$) and enhanced flow focusing upstream of the head-to-wall junction ($W^* > 1$). For $W^* < 1$, flow focusing into the canyon head is limited by the flood width because the backwater length is larger than the flood width. In addition, the zone of maximum flow convergence may be pushed downstream of the head-to-wall junction as described above (Figure 10a). For large W^* and fixed w^*, the radius of the canyon head becomes large with respect to the backwater length, which again is the characteristic length over which flow focusing occurs. Thus, we interpret the reduction in α^*_w for large W^* to be caused by enhanced flow capture in the canyon head, upstream of the head-to-wall junction. Analogously to the acceleration factor ratio at the wall, cumulative head discharge q^* is maximum at $W^* \approx 1$ for subcritical flows (Figure 11c).

Similar to the decrease in acceleration factor ratio at the wall, the acceleration factor ratio at the toe decreases as W^* gets smaller and the toe eventually dries at $W^* \approx 0.5$. However, unlike α^*_w, the acceleration factor ratio at the toe does not decrease with increasing W^* because of the coincident shortening of the canyon which minimizes flow loss upstream (Figure 4).

For supercritical flows, the acceleration factor ratio at the head and wall (Figure 11b) and cumulative head discharge (Figure 11c) are roughly constant, which we interpret as the result of the decreased

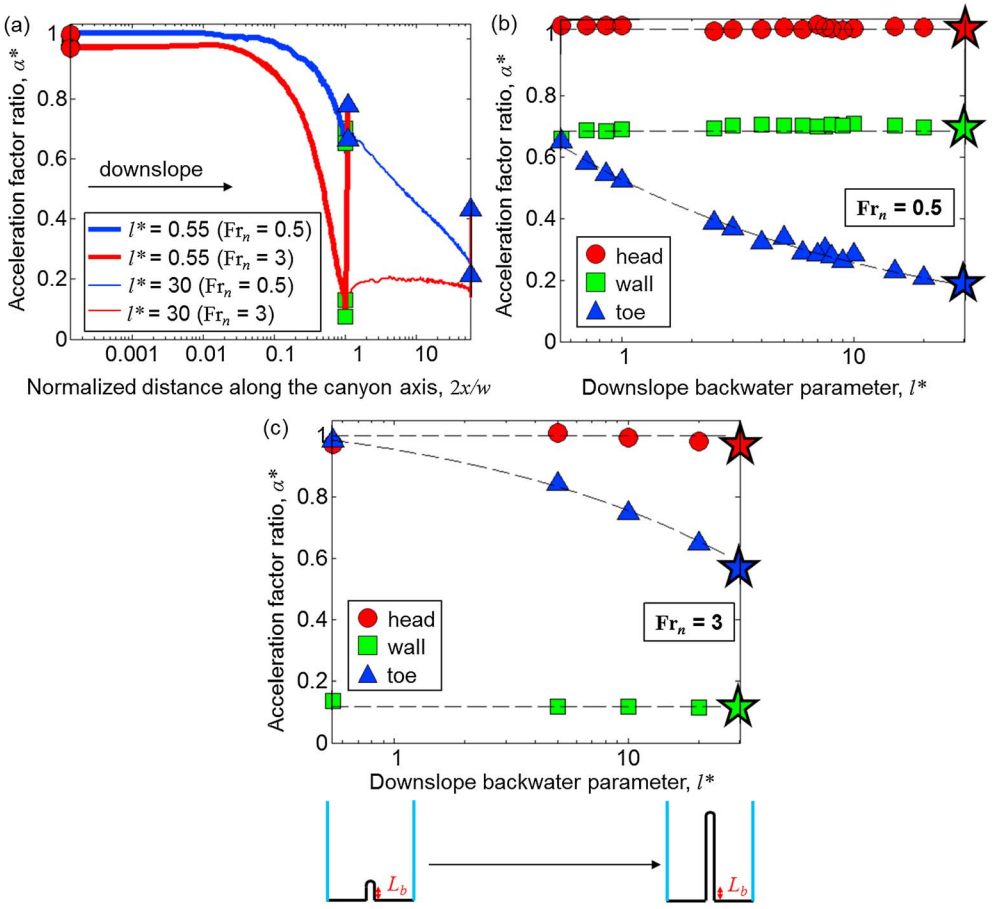

Figure 12. (a) Acceleration factor ratio α^* along the brink of the canyon. The abscissa is the distance measured along the spatial x axis (Figure 3) from the center of the canyon head, normalized by $w/2$, such that this distance equals unity at the head-to-wall junction (i.e., where $\theta = \pi/2$). Blue lines are subcritical runs, whereas red lines are supercritical runs. Thinner lines correspond to the base runs (with $l^* = 30$, Figure 5), while thicker lines have a canyon width to flood width ratio of $l^* = 0.55$. Red circles indicate the canyon head center, green squares the head-to-wall junction, and blue triangles the canyon toe (Figure 3). Note that the acceleration factor at the toe (blue triangle) is measured in the downslope (x) direction and hence is offset from the profile that shows acceleration in cross-slope (y) direction at the corner junction between the canyon and the escarpment. Figures 12b and 12c show the normalized acceleration factor as a function of the downslope backwater parameter l^* for subcritical flows ($\mathrm{Fr}_n = 0.5$) and supercritical flows ($\mathrm{Fr}_n = 3$), respectively. Stars represent the base case simulations. Dashed lines are the best fit solutions discussed in section 5. Sketches at the bottom of Figure 12c illustrate how plan view geometry varies as l^* increases (Figure 4).

importance of lateral backwater effects for supercritical floods. However, the acceleration factor ratio at the toe integrates the backwater effects all along the canyon sidewalls upslope of the toe, and thus, $\alpha*_t$ decreases with decreasing W^* due to water lost to the canyon and drying at the toe for $W^* < 0.3$.

4.5. Experiment Series 4: Downslope Backwater Parameter l^*

In experiment series 4, we investigated the effect of canyon lengthening. We varied the downslope backwater parameter l^* between 0.55 and 30 for two different Froude numbers ($\mathrm{Fr}_n = 0.5$ and $\mathrm{Fr}_n = 3$), with all other parameters set to the base case values ($w^* = 0.1$, $W^* = 4.5$, and $S = 0.0075$, Table 1).

As expected, the acceleration factor ratio around the head and walls does not vary for either subcritical or supercritical floods as l^* increases with all other parameters held constant (Figure 12a). Similarly, cumulative head discharge does not vary with l^* and therefore is not shown.

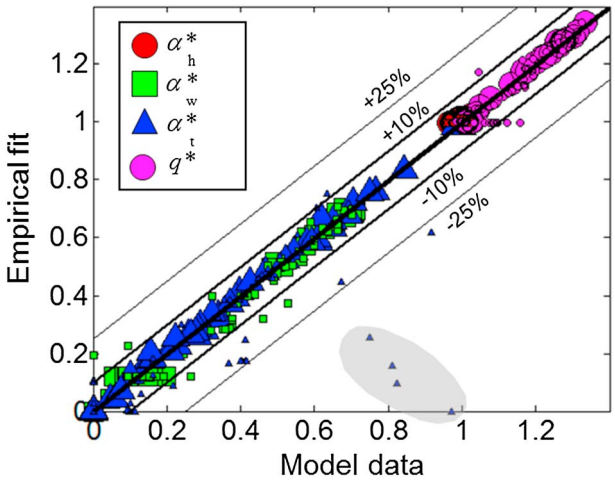

Figure 13. Best fit versus model data (acceleration factor ratios at the head α^*_h, wall α^*_w, and toe α^*_t and normalized cumulative head discharge q^*). Large symbols show runs that were used for the best fit, whereas small ones show runs that were not and have two parameters or more that differ from the base runs (total of $4 \times 110 = 440$ symbols). The thin black lines highlight ±25%, and the intermediate ones indicate ±10%. A perfect fit falls on the 1:1 thick black line. Note that 180 of these symbols represent the test runs (those not taken into account to derive the semiempirical fits), and their vast majority fall within ±10% of the values predicted by equations (A1)–(A8). Toe accelerations highlighted in gray correspond to wide ($w^* \geq 0.75$), short canyons ($l^* \leq 6$) in supercritical floods. In this configuration, acceleration at the toe is high due to the high downslope inertia of the flow and the little amount of water lost to the walls in the cross-slope direction. Our scaling underestimates the acceleration at the toe in this configuration.

In contrast to the head and sidewalls, the acceleration factor at the toe is larger for relatively short canyons (smaller l^*). We interpret this trend as the result of water pouring over a shorter sidewall distance, and thus, less water is lost along the walls for smaller canyons (Figure 12a). For subcritical floods, we observe a rapid decrease in acceleration at the toe as canyons lengthen (Figure 12b). For supercritical floods, the reduction in acceleration factor ratio at the toe with increasing l^* is more gradual due to less water lost into the canyon upstream (Figure 12c).

5. Semiempirical Approximations

Because our 2-D hydraulic simulations are computationally demanding, it is of interest to obtain semiempirical approximations to our results in order to predict the acceleration factor ratios and cumulative head discharge, α^*_h, α^*_w, α^*_t, and q^*, as a function of Fr_n, w^*, W^*, and l^* in a way analogous to equation (1). All parameters affect the acceleration factor ratios roughly independently. We were able to fit the data by addressing each parameter separately in the regime where other parameters do not matter through multiple nonlinear regressions. The fit relationships are given in Appendix A.

We first corrected the data for Froude number Fr_n by dividing the data by exponential or power function fits to experiment series 1. We then identified and ranked by decreasing importance the other dimensionless parameters driving the remaining variance (w^* then W^* for α^*_w and q^*; l^* then W^* then w^* for α^*_t). Finally, we sequentially corrected for the variance induced by each of the ranked parameters by further dividing the data by the corresponding power law fits. When different functional fits were needed for different parameter ranges, we attempted to impose continuity of the fit across the range boundaries. Nevertheless, discontinuities in the fits still arise in cases because we did not model every possible combination of parameters.

Figure 13 shows a comparison between the acceleration factor ratios and cumulative head discharge as predicted by ANUGA and the best fit functions we derived. The root mean square error (RMS) between the fits and the data is equal to 1.1%. In order to test the ability of the semiempirical fits to predict acceleration factor ratios and cumulative head discharge for parameter values that were not used when performing the fits, we designed a set of 45 additional test simulations that explored various other combinations of parameter values (Table 1). The fit functions are successful at predicting most of the additional simulations (Figure 13). The functions, however, did not fit as well α^*_w for supercritical floods at canyons that are relatively short and wide (shaded in gray in Figure 13), a configuration we did not explore extensively. The RMS between the additional test data and their fits is equal to 2.2% when the latter simulations are excluded and to 4.1% when they are included.

Because Fr_n, W^*, and l^* have no upper limit by definition, one might be interested in a case outside our explored parameter space. In most applications, the Froude number Fr_n falls within our modeled range. Higher Froude numbers would have acceleration factor ratios of unity at the head and zero at the wall due to the near absence

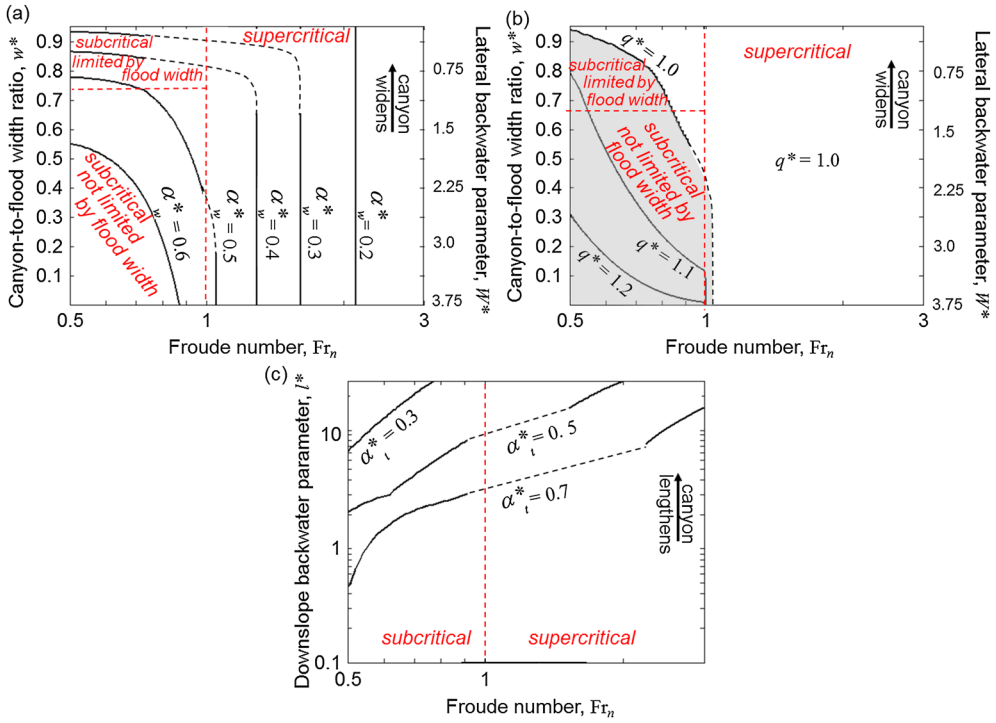

Figure 14. (a) Wall acceleration factor ratio α^*_w and (b) normalized cumulative head discharge q^* contours for the case of canyon widening, where both the canyon-to-flood width ratio w^* and the lateral backwater limitation factor W^* change ($l^* = 30$, $S = 0.0075$). The shaded area shows the parameter space where cumulative head discharge is enhanced ($q^* \geq 1$). As a canyon widens, one moves upward on the plots. (c) Toe acceleration factor ratio α^*_t for the case of canyon lengthening ($w^* = 0.1$, $W^* = 4.5$, $S = 0.0075$). As a canyon lengthens, l^* increases and one moves upward on the plot. Contours are determined from the semiempirical fits (equations (A1)–(A8)). Dashed lines represent expected trends where semiempirical fits produce discontinuities.

of flow focusing. At the toe, its value would still vary greatly with the amount of water lost along the canyon sidewalls, and thus with the downslope backwater parameter l^*. The flood width limitation factor W^* does not significantly affect the hydraulics at values higher than the range we tested (at $W^* = 5$, acceleration factor ratios at the wall do not vary significantly, and normalized cumulative head discharge decreases to unity). In cases where $\mathrm{Fr}_n < 1$ and W^* are very small, one can assume that α^*_w and α^*_t are small. Finally, almost no water is left at the toe of very long canyons ($l^* \gg 1$), such that α^*_t can be assumed to be zero. Most of these end member cases are reproduced by the fits. When the fits predict negative values for acceleration factor ratios, they should be set to zero.

6. Discussion

6.1. Flow Regimes

Figure 14 illustrates how the best fit functions can be used to predict the acceleration factor around the brink of horseshoe waterfalls that widen and lengthen. Because the normalizing denominator for the acceleration factor ratios (α_{1D}, equation (1)) and the cumulative head discharge ($q_n w/2$) can be calculated independently, one can invert for dimensional properties of the flow from the best fit equations (equations (A1)–(A8)).

The effect of increasing the canyon width is best described by the acceleration factor ratio at the wall α^*_w and the cumulative head discharge q^* (Figures 14a and 14b). In natural systems with a normal flow depth that is constant over time, canyon widening will not only cause w^* to increase but also cause W^* to decrease, and flow around the canyon brink will be affected by lateral backwater effects. Figures 14a and 14b show how

α^*_w and q^* can be summarized in several flow regimes with coincident changes in w^* and W^*. In the subcritical regime ($Fr_n < 1$) with focusing not limited by the width of the flood ($W^* > 1$), acceleration at the wall is mostly a function of Froude number, and cumulative head discharge is enhanced. As the canyon widens ($W^* < 1$), acceleration at the wall is mostly a function of canyon width and α^*_w decreases. Likewise, with canyon widening, the cumulative head discharge goes from enhanced with respect to the 1-D case ($q^* > 1$) to normal ($q^* = 1$). In the supercritical regime, acceleration at the wall is a function of the flood Froude number only and decreases with increasing Fr_n. Head discharge for supercritical floods is roughly equal to the corresponding 1-D discharge.

Canyon lengthening affects mostly the acceleration factor at the toe α^*_t (Figure 14c). Acceleration at the toe is reduced with larger canyons; however, this effect weakens at higher Froude numbers.

6.2. Engineering Applications

Hydraulic engineers typically employ full 3-D numerical models to study and design specific spillways with complex geometries [e.g., *Feurich et al.*, 2011]. Nevertheless, our results have implications for the early stages of designing spillways. A first important result of our modeling is that the acceleration factor ratio at the head of a horseshoe waterfall is only enhanced by less than 4% compared to the 1-D case as long as there is no cross-stream topographic gradient (e.g., Figure 7). Consequently, in applications where the required precision is of a few percent, it can be assumed that acceleration at the head can be approximated by equation (1).

Moreover, understanding flow focusing is essential to optimize the discharge into the head of the canyon. For example, one might need to minimize erosion at the base of a horseshoe spillway. This can be accomplished by decreasing the amount of flow focusing toward the canyon, and thus the velocity and width of the jet impinging the plunge pool. If flow focusing is minimized, by making the canyon as wide as the flood ($w^* \approx 1$), the discharge per unit width at the center of the spillway will be that of the linear escarpment, and the discharge will be lower everywhere else along the brink, stabilizing the sidewalls. If enhanced discharge is desired to increase the generated power of a water turbine, a horseshoe spillway should be narrower than the total flood width ($w^* \ll 1$) such that flow focusing is maximum at the tip of the horseshoe (e.g., $W^* \approx 1$). Our results suggest that this design can enhance discharge by up to about 35% (e.g., Figure 7). Because hydropower is proportional to discharge [e.g., *Sayers*, 1990], such a design could increase energy production.

6.3. Implications for the Shape of Canyon Heads and Canyon Dynamics

Waterfalls retreat upstream as a consequence of erosion at the knickpoint, causing formation of canyons. Erosion occurs either through undercutting in the plunge pool or through plucking and toppling of rock blocks upstream of the brink [e.g., *Gilbert*, 1907; *Haviv et al.*, 2006; *Lamb et al.*, 2006, 2007; *Lamb and Dietrich*, 2009; *Mackey et al.*, 2014]. Undercutting occurs as a result of scouring of rocks where the water jet impinges the plunge pool, by the combined mechanical action of water and transported sediments [e.g., *Stein and Julien*, 1993; *Flores-Cervantes et al.*, 2006]. In particular, *Flores-Cervantes et al.* [2006] showed that bed shear stress at the base of the jet increases with flow velocity at the brink U_0. Moreover, higher water discharges cause higher sediment capacity of the flow [e.g., *Meyer-Peter and Muller*, 1948; *Fernandez Luque and Van Beek*, 1976], which enhances plunge pool erosion. Consequently, more focusing toward the canyon head suggests that more erosional work is accomplished by water and sediment. Enhanced erosion at the head combined with drying of the sidewalls promotes upstream propagation of the canyon head as opposed to canyon widening. Our results indicate that higher head discharges are obtained for lower Froude numbers, and lateral backwater lengths smaller than the half flooded width.

Plucking and toppling occur through the action of bed shear stress applied by water flow upstream of the waterfall brink [e.g., *Coleman et al.*, 2003; *Chatanantavet and Parker*, 2009]. The bed shear stress at the brink is given by

$$\tau_b = \rho C_f {U_p}^2 = \rho C_f \alpha^{*2} {U_n}^2 \tag{8}$$

where ρ is the density of water and thus scales with the acceleration factor ratio squared. Assuming that erosion rate is proportional to bed shear stress to some positive power [e.g., *Howard and Kerby*, 1983], higher

acceleration factor ratios should lead to higher erosion rate [*Stein and Julien*, 1993; *Haviv et al.*, 2006; *Lamb and Dietrich*, 2009].

Our modeling suggests that flow focusing enhances acceleration factor ratios around the head of canyons for low Froude numbers, and low lateral backwater lengths (equations (A1), (A2), (A4), and (A5)), and decreases acceleration factor ratios along the walls and toes as canyons lengthen and widen (equations (A2)–(A7)). If we make the assumption that erosion only occurs when a certain threshold shear stress is surpassed [e.g., *Lamb and Dietrich*, 2009], erosion is more likely to prevail where α^* is higher. Consequently, different combinations of bed shear stress at the head and at the head-to-wall junction may determine whether the canyon widens or narrows, while bed shear stress at the head and the toe may control whether the canyon grows or shrinks.

We showed that plan view curvature of the canyon rim drives cross-slope flow, and thus convergence of the flood waters toward the canyon. Flow focusing can in turn drive the creation of more curvature. Indeed, variations in flow velocities around the brink may lead to variable erosion rates around the brink, with higher erosion rates at the canyon head where velocities are enhanced and decreased erosion rates along the walls where velocities are decreased [e.g., *Stein and Julien*, 1993; *Lamb and Dietrich*, 2009]. Consequently, feedbacks between flood hydraulics and canyon form may be similar to those observed in the formation of amphitheater heads by groundwater sapping in sand [*Howard and McLane*, 1988] and may help to explain the origin of amphitheater-headed canyons in competent rock [e.g., *Lamb et al.*, 2006, 2014] (Figure 1). It is likely that canyon head shape differs for different degrees of focusing and thus might be a function of flood attributes, such as Froude number Fr_n and flood width limitation factor W^*. This conclusion modifies that of *Petroff et al.* [2011], who proposed that erosion rates are proportional to local plan view curvature of a canyon head. Our results suggest that erosion may be enhanced at the center of the canyon head due to flow focusing even in the absence of spatial changes in curvature (as in our case of a semicircular head).

7. Conclusion

Horseshoe-shaped waterfalls modify the flow patterns upstream of waterfalls, flow acceleration at the waterfall brink, and cumulative discharge into the waterfall. The distribution of the acceleration factor around the canyon brink is mainly controlled by the normal flow Froude number, the width of the flood compared to its lateral backwater length and the canyon width, and the downslope length of the canyon relative to the backwater length.

In the case of a sheet flood, that is, when the canyon is much narrower than the flood and lateral backwater effects do not limit flow focusing, the acceleration factor is entirely determined by the Froude number and the length of the canyon. Higher Froude numbers decrease the amount of focusing and thus decrease the acceleration factor around the canyon sidewalls (i.e., $\alpha^*_w \to 0$ for $\mathrm{Fr}_n \gg 1$), increase it at the canyon toe, and lower the cumulative discharge into the canyon head. Longer canyons lose more water along their sidewalls than shorter canyons and thus have decreased acceleration factors at the canyon toe.

For nonsheet floods, the flow patterns are more complicated due to the influence of boundaries that limit flow focusing into the waterfall. Generally, wider waterfalls and/or higher lateral backwater lengths decrease both the acceleration factor around the canyon head and walls and the cumulative discharge into the canyon head. When the canyon is confined within the full width of the flood ($W^* \approx 1$), the walls and the toe are at the same location, and the acceleration factor in both the cross-slope and downslope directions is zero $\left(\alpha^*_w \approx \alpha^*_t \approx 0\right)$. Finally, when the lateral backwater limitation factor is much smaller than unity ($W^* \ll 1$), the acceleration factor along the walls tends to zero $\left(\alpha^*_w \to 0\right)$.

The semiempirical relationships we derived to relate acceleration and discharge around the brink of waterfalls may provide some guidance during the early stages of spillway design and optimization. These relationships also provide a quantitative understanding of flow focusing that can be used to help explain the shape of waterfalls, as well as their evolution.

Appendix A: Fit Relationships

The acceleration factor ratio at the head α^*_h decreases with Froude number Fr_n for subcritical floods and is roughly equal to unity for supercritical floods.

$$\alpha^*_h = \begin{cases} 1 + 0.05(1 - Fr_n)^{1.65} & \text{for } \mathrm{Fr}_n < 1 \\ 1 & \text{for } \mathrm{Fr}_n \geq 1 \end{cases} \tag{A1}$$

In the case of a sheet flood ($w^* \ll 1$ and $W^* > 1$), the acceleration factor ratio at the wall α^*_w decreases with Froude number Fr_n, and the decrease is steeper for Fr_n between 1 and 3.

$$\alpha^*_{w,sf} = 1.47\exp\left[-\left(\frac{\mathrm{Fr}_n + 1.18}{1.58}\right)^2\right] - 0.53\exp\left[-\left(\frac{\mathrm{Fr}_n + 0.03}{0.53}\right)^2\right] + 85550\exp\left[-\left(\frac{\mathrm{Fr}_n + 51}{14.7}\right)^2\right] \tag{A2}$$

For a sheet flood, the acceleration factor ratio at the toe α^*_t increases with Froude number Fr_n and decreases with the downslope backwater parameter I^*.

$$\alpha^*_{t,sf} = \begin{cases} \left(2.08\mathrm{Fr}_n^{0.11} - 1.76\right)\left(3.68I^{*-0.31}\right) & \text{for } \mathrm{Fr}_n < 1 \\ \left(2.08\mathrm{Fr}_n^{0.11} - 1.76\right)\left(2.02 - 0.29I^{*0.35}\right) & \text{for } \mathrm{Fr}_n \geq 1 \end{cases} \tag{A3}$$

For subcritical nonsheet floods, the acceleration factor at the wall α^*_w decreases with the canyon width to flood width ratio w^* and increases with the flood width limitation factor W^* (as long as $W^* < 1$). For supercritical nonsheet floods, the acceleration factor ratio at the wall α^*_w slightly increases with canyon width to flood width ratio w^*.

$$\alpha^*_w = \begin{cases} \alpha^*_{w,sf}\left(1 - w^*\right)^{0.22} G_1 & \text{for } \mathrm{Fr}_n < 1 \\ \alpha^*_{w,sf} & \text{for } \mathrm{Fr}_n \geq 1 \end{cases} \tag{A4}$$

in which

$$G_1 = \begin{cases} \left[1.06 - 0.38(1 - W^*)^{1.41}\right] & \text{for } W^* < 1 \\ \left[1.07 - 7.72\times10^{-3}W^*\right] & \text{for } W^* \geq 1 \end{cases} \tag{A5}$$

The acceleration factor ratio at the toe α^*_t for subcritical nonsheet floods increases with w^* and decreases with W^*. For supercritical nonsheet floods, the acceleration factor ratio at the toe α^*_t increases with both w^* and W^*.

$$\alpha^*_t = \begin{cases} \alpha^*_{t,sf}\left(0.87 - 21.75w^{*4.65}\right)\left[1.18\exp(0.01W^*) - 1.39\exp(-0.38W^*)\right] & \text{for } \mathrm{Fr}_n < 1 \\ \alpha^*_{t,sf}\left(1 + 0.68w^{*5.09}\right)\left[1.07 - 1.21\exp(-0.49W^*)\right] & \text{for } \mathrm{Fr}_n \geq 1 \end{cases} \tag{A6}$$

Normalized cumulative head discharge q^* decreases with Froude number Fr_n, increases and then decreases with flood width limitation factor W^*, and either decreases or is constant with canyon width to flood width ratio w^* depending on whether the flood is subcritical or supercritical.

$$q^* = \begin{cases} \left[1 + 0.79\exp(-2.16Fr_n)\right]\left(1.14 - 0.33w^{*0.37}\right)G_2 & \text{for } \mathrm{Fr}_n < 1 \\ \left[1 + 0.79\exp(-2.16Fr_n)\right] & \text{for } \mathrm{Fr}_n \geq 1 \end{cases} \tag{A7}$$

in which

$$G_2 = \begin{cases} 1.03 - 0.16(1 - W^*)^{2.85} & \text{for } W^* < 1 \\ 1.08 - 0.04W^{*0.31} & \text{for } W^* \geq 1 \end{cases} \tag{A8}$$

Note that these fit relationships are valid for the tested range and combinations of dimensionless parameters listed in Table 1 but should be used with caution when applied near the edges of the parameter ranges modeled in this study for nonsheet floods. They were tested against test simulations that encompassed different parameter combinations (Figure 13 and Table 1) and are yet to be validated outside of the modeled ranges. Nevertheless, most of the acceleration factor ratios have predictable asymptotical behaviors (section 5).

Notations

C_f	dimensionless friction coefficient
Fr	Froude number
Fr_n	normal Froude number
Fr_0	Froude number at the rim
g	acceleration of gravity (m/s^2)
h	flow depth (m)
h_c	critical flow depth (m)
h_n	normal flow depth (m)
h_0	flow depth at the brink (m)
l	canyon length (m)
l^*	downslope backwater parameter
L_b	backwater length (m)
n	Manning's n (s/m$^{1/3}$)
q	discharge per unit width (m^2/s)
q_n	upstream discharge per unit width (m^2/s)
q_0	discharge per unit width at the brink (m^2/s)
q^*	normalized cumulative head discharge
Q_h	total discharge within the canyon head (m^3/s)
Q_n	normal discharge flowing across a width of a canyon radius (m^3/s)
r	ratio of flow depth to normal flow depth
S	bed slope upstream of the waterfall
t	time (s)
U	depth-averaged flow velocity (m/s)
U_n	depth-averaged normal flow velocity (m/s)
U_p	depth-averaged flow velocity perpendicular to the brink (m/s)
U_x	depth-averaged downslope component of flow velocity (m/s)
U_y	depth-averaged cross-slope component of flow velocity (m/s)
U_0	depth-averaged flow velocity at the brink (m/s)
u^*	shear velocity (m/s)
w	canyon width (m)
w^*	canyon-to-flood width ratio
W^*	lateral backwater flood width limitation factor
W	flood width (m)
x	downslope spatial coordinate (m)
y	cross-slope spatial coordinate (m)
$\alpha_{1\mathrm{D}}$	acceleration factor at the brink of a 1-D step
$\alpha_{2\mathrm{D}}$	acceleration factor at the brink of a 2-D canyon
α^*	acceleration factor ratio
α^*_h	acceleration factor ratio at the head center
α^*_w	acceleration factor ratio at the head-to-wall junction
α^*_t	acceleration factor ratio at the canyon toe
$\alpha^*_{w,sf}$	acceleration factor ratio at the head-to-wall junction for a sheet flood
$\alpha^*_{t,sf}$	acceleration factor ratio at the canyon toe for a sheet flood
ε	fractional acceleration caused by nonhydrostatic pressure at the rim

θ azimuth with respect to the canyon centerline
ρ density of water (kg/m^3)
τ_b bed shear stress (N/m^2)

Acknowledgments
This work benefited from discussion with Gary Parker, Gareth Davies, and Stephen Roberts. We thank Cailan Haliday for assistance with and testing of the numerical model setup. We also thank three anonymous reviewers for helpful and constructive reviews that improved this paper. Support was provided by the NASA Earth and Space Science Fellowship 12-PLANET12F-0071, NSF Grant EAR-1147381, and NASA Grant NNX13AM83G. All data in the present paper are available upon request to the corresponding author.

References

Alonso, C. V., S. J. Bennett, and O. R. Stein (2002), Predicting head cut erosion and migration in concentrated flows typical of upland areas, *Water Resour. Res.*, *38*(12), 1303, doi:10.1029/2001WR001173.
Annandale, G. (1995), Erodibility, *J. Hydraul. Res.*, *33*(4), 471–494.
Baker, V. R., and D. J. Milton (1974), Erosion by catastrophic floods on Mars and Earth, *Icarus*, *23*(1), 27–41.
Barnes, M. P., and T. E. Baldock (2006), Bed shear stress measurements in dam break and swash flows, paper presented at International Conference on Civil and Environmental Engineering (ICCEE-2006).
Baynes, E. R. C., M. Attal, S. Niedermann, L. A. Kirstein, A. J. Dugmore, and M. Naylor (2015), Erosion during extreme flood events dominates Holocene canyon evolution in northeast Iceland, *Proc. Natl. Acad. Sci. U.S.A.*, *112*(8), 2355–2360, doi:10.1073/pnas.1415443112.
Bennett, S. J. (1999), Effect of slope on the growth and migration of headcuts in rills, *Geomorphology*, *30*(3), 273–290.
Bennett, S. J., and J. Casali (2001), Effect of initial step height on headcut development in upland concentrated flows, *Water Resour. Res.*, *37*(5), 1475–1484, doi:10.1029/2000WR900373.
Bishop, P., T. B. Hoey, J. D. Jansen, and I. L. Artza (2005), Knickpoint recession rate and catchment area: the case of uplifted rivers in Eastern Scotland, *Earth Surf. Processes Landforms*, *30*(6), 767–778.
Bresse, J. A. C. (1860), *Cours de Mecanique Appliquee: Professe a l'Ecole Imperiale des Ponts et Chaussees. Hydraulique*, Gauthier-Villars, Paris.
Bretz, J. H. (1969), The Lake Missoula floods and the channeled scabland, *J. Geol.*, *77*(5), 505–543.
Brush, L. M., and M. G. Wolman (1960), Knickpoint behavior in noncohesive material: A laboratory study, *Geol. Soc. Am. Bull.*, *71*(1), 59–74.
Butcher, J. C. (2008), *Numerical Methods for Ordinary Differential Equations*, John Wiley, Chichester, U. K.
Chanson, H. (1994), Hydraulics of nappe flow regime above stepped chutes and spillways, *Aust. Civ. Struct. Eng. Trans.*, *CE36*(1), 69–76.
Chanson, H. (1995), *Hydraulic Design of Stepped Cascades, Channels, Weirs and Spillways*, Pergamon, Oxford, U. K.
Chanson, H. (2002), *Hydraulics of Stepped Chutes and Spillways*, CRC Press, Balkema, Lisse, Netherlands.
Chatanantavet, P., and G. Parker (2009), Physically based modeling of bedrock incision by abrasion, plucking, and macroabrasion, *J. Geophys. Res.*, *114*, F04018, doi:10.1029/2008JF001044.
Chow, V. (1959), *Open Channel Hydraulics*, McGraw-Hill Book Company, Inc., New York.
Coleman, S. E., B. W. Melville, and L. Gore (2003), Fluvial entrainment of protruding fractured rock, *J. Hydraul. Eng.*, *129*(11), 872–884.
Costa, J. E. (1987), Hydraulics and basin morphometry of the largest flash floods in the conterminous United States, *J. Hydrol.*, *93*(3), 313–338.
Craddock, R. A., A. D. Howard, R. P. Irwin, S. Tooth, R. M. Williams, and P.-S. Chu (2012), Drainage network development in the Keanakako'i tephra, Kilauea Volcano, Hawai'i: Implications for fluvial erosion and valley network formation on early Mars, *J. Geophys. Res.*, *117*, E08009, doi:10.1029/2012JE004074.
Delleur, J., J. Dooge, and K. Gent (1956), Influence of slope and roughness on the free overfall, *J. Hydraul. Div., Am. Soc. Civ. Eng.*, *82*(4), 1–35.
DiBiase, R. A., K. X. Whipple, M. P. Lamb, and A. M. Heimsath (2014), The role of waterfalls and knickzones in controlling the style and pace of landscape adjustment in the western San Gabriel Mountains, California, *Geol. Soc. Am. Bull.*, *127*(3/4), 539–559, doi:10.1130/B31113.1.
Dietrich, W. E., and T. Dunne (1993), The channel head, in *Channel Network Hydrology*, edited by K. Beven and M. J. Kirkby, pp. 175–219, John Wiley, Chichester, U. K.
Dubinski, I. M., and E. Wohl (2013), Relationships between block quarrying, bed shear stress, and stream power: A physical model of block quarrying of a jointed bedrock channel, *Geomorphology*, *180*, 66–81.
Fernandez Luque, R., and R. Van Beek (1976), Erosion and transport of bed-load sediment, *J. Hydraul. Res.*, *14*(2), 127–144.
Feurich, R., F. Kettner, and N. Olsen (2011), Three-dimensional numerical investigation of spillway and reservoir hydraulics, paper presented at Proceedings of the 34th World Congress of the International Association for Hydro-environment Research and Engineering: 33rd Hydrology and Water Resources Symposium and 10th Conference on Hydraulics in Water Engineering, Engineers Australia.
Flint, J.-J. (1973), Experimental development of headward growth of channel networks, *Geol. Soc. Am. Bull.*, *84*(3), 1087–1094.
Flores-Cervantes, J. H., E. Istanbulluoglu, and R. L. Bras (2006), Development of gullies on the landscape: A model of headcut retreat resulting from plunge pool erosion, *J. Geophys. Res.*, *111*, F01010, doi:10.1029/2004JF000226.
Gardner, T. W. (1983), Experimental study of knickpoint and longitudinal profile evolution in cohesive, homogeneous material, *Geol. Soc. Am. Bull.*, *94*(5), 664–672.
Gilbert, G. K. (1907), The rate of recession of Niagara Falls, *U.S. Geol. Surv. Bull.*, *306*, 1–31.
Hager, W., and D. D. K. Hutter (1984), Approximate treatment of plane channel flow, *Acta Mech.*, *51*(1–2), 31–48.
Hager, W. H. (1983), Hydraulics of plane free overfall, *J. Hydraul. Eng.*, *109*(12), 1683–1697.
Hancock, G. S., R. S. Anderson, and K. X. Whipple (1998), Beyond power: Bedrock river incision process and form, in *Rivers Over Rock: Fluvial Processes in Bedrock Channels*, pp. 35–60, AGU, Washington, D. C.
Haviv, I., Y. Enzel, K. Whipple, E. Zilberman, J. Stone, A. Matmon, and L. Fifield (2006), Amplified erosion above waterfalls and oversteepened bedrock reaches, *J. Geophys. Res.*, *111*, F04004, doi:10.1029/2006JF000461.
Howard, A. D., and G. Kerby (1983), Channel changes in badlands, *Geol. Soc. Am. Bull.*, *94*(6), 739–752.
Howard, A. D., and C. F. McLane (1988), Erosion of cohesionless sediment by groundwater seepage, *Water Resour. Res.*, *24*(10), 1659–1674, doi:10.1029/WR024i010p01659.
Howard, A. D., W. E. Dietrich, and M. A. Seidl (1994), Modeling fluvial erosion on regional to continental scales, *J. Geophys. Res.*, *99*(B7), 13971–13986, doi:10.1029/94JB00744.
Izumi, N., and G. Parker (1995), Inception of channelization and drainage basin formation: Upstream-driven theory, *J. Fluid Mech.*, *283*, 341–363.
Izumi, N., and G. Parker (2000), Linear stability analysis of channel inception: Downstream-driven theory, *J. Fluid Mech.*, *419*, 239–262.
Kurganov, A., S. Noelle, and G. Petrova (2001), Semidiscrete central-upwind schemes for hyperbolic conservation laws and Hamilton-Jacobi equations, *SIAM J. Sci. Comput.*, *23*(3), 707–740.
Lamb, M. P., and W. E. Dietrich (2009), The persistence of waterfalls in fractured rock, *Geol. Soc. Am. Bull.*, *121*(7–8), 1123–1134.
Lamb, M. P., A. D. Howard, J. Johnson, K. X. Whipple, W. E. Dietrich, and J. T. Perron (2006), Can springs cut canyons into rock?, *J. Geophys. Res.*, *111*, E07002, doi:10.1029/2005JE002663.

Lamb, M. P., A. D. Howard, W. E. Dietrich, and J. T. Perron (2007), Formation of amphitheater-headed valleys by waterfall erosion after large-scale slumping on Hawai'i, *Geol. Soc. Am. Bull.*, *119*(7–8), 805–822.
Lamb, M. P., W. E. Dietrich, S. M. Aciego, D. J. DePaolo, and M. Manga (2008), Formation of Box Canyon, Idaho, by megaflood: Implications for seepage erosion on Earth and Mars, *Science*, *320*(5879), 1067–1070.
Lamb, M. P., J. A. Nittrouer, D. Mohrig, and J. Shaw (2012), Backwater and river plume controls on scour upstream of river mouths: Implications for fluvio-deltaic morphodynamics, *J. Geophys. Res.*, *117*, F01002, doi:10.1029/2011JF002079.
Lamb, M. P., B. H. Mackey, and K. A. Farley (2014), Amphitheater-headed canyons formed by megaflooding at Malad Gorge, Idaho, *Proc. Natl. Acad. Sci. U.S.A.*, *111*(1), 57–62.
Leopold, L. B., and W. B. Bull (1979), Base level, aggradation, and grade, *Proc. Am. Philos. Soc.*, 168–202.
Mackey, B. H., J. S. Scheingross, M. P. Lamb, and K. A. Farley (2014), Knickpoint formation, rapid propagation, and landscape response following coastal cliff retreat at the last interglacial sea-level highstand: Kaua'i, Hawai'i, *Geol. Soc. Am. Bull.*, *126*, 925–942.
Meyer-Peter, E., and R. Muller (1948), Formulas for bed-load transport, paper presented at Proceedings of the 2nd Meeting of the International Association for Hydraulic Structures Research, International Association of Hydraulic Research Delft.
Mungkasi, S., and S. G. Roberts (2011), A finite volume method for shallow water flows on triangular computational grids, paper presented at 2011 International Conference on Advanced Computer Science and Information System (ICACSIS), IEEE.
Mungkasi, S., and S. G. Roberts (2013), Validation of ANUGA hydraulic model using exact solutions to shallow water wave problems, *J. Phys. Conf. Ser.*, *423*, 012029.
Nielsen, O., S. Roberts, D. Gray, A. McPherson, and A. Hitchman (2005), Hydrodynamic modelling of coastal inundation, paper presented at MODSIM 2005 International Congress on Modelling and Simulation.
O'Connor, J. E. (1993), Hydrology, hydraulics, and geomorphology of the Bonneville flood, *Geol. Soc. Am. Spec. Pap.*, *274*, 1–84.
Pasternack, G. B., C. R. Ellis, K. A. Leier, B. L. Valle, and J. D. Marr (2006), Convergent hydraulics at horseshoe steps in bedrock rivers, *Geomorphology*, *82*(1), 126–145.
Pasternack, G. B., C. R. Ellis, and J. D. Marr (2007), Jet and hydraulic jump near-bed stresses below a horseshoe waterfall, *Water Resour. Res.*, *43*, W07449, doi:10.1029/2006WR005774.
Petroff, A. P., O. Devauchelle, D. M. Abrams, A. E. Lobkovsky, A. Kudrolli, and D. H. Rothman (2011), Geometry of valley growth, *J. Fluid Mech.*, *673*, 245–254, doi:10.1017/s002211201100053x.
Rajaratnam, N., and D. Muralidhar (1968), Characteristics of the rectangular free overfall, *J. Hydraul. Res.*, *6*(3), 233–258.
Rengers, F. K., and G. Tucker (2014), Analysis and modeling of gully headcut dynamics, North American high plains, *J. Geophys. Res. Earth Surf.*, *119*, 983–1003, doi:10.1002/2013JF002962.
Roberts, S., O. Nielsen, and J. Jakeman (2008), Simulation of tsunami and flash floods, in *Modeling, Simulation and Optimization of Complex Processes*, edited, pp. 489–498, Springer, Berlin.
Roberts, S., O. Nielsen, D. Gray, and J. Sexton (2009), *ANUGA User Manual*, Commonwealth of Australia (Geoscience Australia) and the Australian National University, Canberra.
Rouse, H. (1936), Discharge characteristics of the free overfall, *Civ. Eng.*, *6*, 257–260.
Rouse, H. (1937), Pressure distribution and acceleration at the free overfall, *Civ. Eng.*, *7*(7), 518.
Rouse, H. (1950), *Engineering Hydraulics*, John Wiley, New York.
Sayers, A. T. (1990), *Hydraulic and Compressible Flow Turbomachines*, McGraw-Hill, London.
Stein, O. R., and P. Julien (1993), Criterion delineating the mode of headcut migration, *J. Hydraul. Eng.*, *119*(1), 37–50.
Stein, O. R., and D. A. LaTray (2002), Experiments and modeling of head cut migration in stratified soils, *Water Resour. Res.*, *38*(12), 1284, doi:10.1029/2001WR001166.
Stein, O. R., P. Julien, and C. Alonso (1993), Mechanics of jet scour downstream of a headcut, *J. Hydraul. Res.*, *31*(6), 723–738.
Tokyay, N. D., and D. Yildiz (2007), Characteristics of free overfall for supercritical flows, *Can. J. Civ. Eng.*, *34*(2), 162–169.
Tucker, G. E., L. Arnold, R. L. Bras, H. Flores, E. Istanbulluoglu, and P. Solyom (2006), Headwater channel dynamics in semiarid rangelands, Colorado High Plains, USA, *Geol. Soc. Am. Bull.*, *118*(7–8), 959–974.
Warner, N. H., S. Gupta, J.-R. Kim, S.-Y. Lin, and J.-P. Muller (2010), Retreat of a giant cataract in a long-lived (3.7–2.6 Ga) Martian outflow channel, *Geology*, *38*(9), 791–794.
Whipple, K. X., G. S. Hancock, and R. S. Anderson (2000), River incision into bedrock: Mechanics and relative efficacy of plucking, abrasion, and cavitation, *Geol. Soc. Am. Bull.*, *112*(3), 490–503.
Williams, R. M., and M. C. Malin (2004), Evidence for late stage fluvial activity in Kasei Valles, Mars, *J. Geophys. Res.*, *109*, E06001, doi:10.1029/2003JE002178.
Wohl, E. (2008), The effect of bedrock jointing on the formation of straths in the Cache la Poudre River drainage, Colorado Front Range, *J. Geophys. Res.*, *113*, F01007, doi:10.1029/2007JF000817.
Zoppou, C., and S. Roberts (1999), Catastrophic collapse of water supply reservoirs in urban areas, *J. Hydraul. Eng.*, *125*(7), 686–695.